1    **Where does the dust deposited over the Sierra Nevada snow come from?**

3    Huilin Huang[1*], Yun Qian[1*], Ye Liu[1], Cenlin He[2], Jianyu Zheng[3,4], Zhibo Zhang[3,4], Antonis Gkikas[5]

5    [1]Atmospheric Sciences and Global Change Division, Pacific Northwest National Laboratory, Richland, WA,

6    USA

7    [2]Research Applications Laboratory, National Center for Atmospheric Research, Boulder, CO, USA

8    [3]Department of Physics, University of Maryland Baltimore County, Baltimore, MD, USA

9    [4]Joint Center for Earth Systems Technology, University of Maryland Baltimore County, Baltimore, MD, USA

10   [5]Institute for Astronomy, Astrophysics, Space Applications and Remote Sensing, National Observatory of

11   Athens, Athens, Greece

13   *Corresponding to: Huilin Huang, Huilin.huang@pnnl.gov; Yun Qian, Yun.Qian@pnnl.gov

17   Submitted to Atmospheric Chemistry and Physics

**Abstract**

Mineral dust contributes up to one-half of surface aerosol loading in spring over the southwestern U.S., posing an environmental challenge that threatens human health and the ecosystem. Using the self-organizing map (SOM) analysis with dust deposition and fluxes data from WRF-Chem and Modern-Era Retrospective analysis for Research and Applications, Version 2 (MERRA-2), we identify four typical dust transport patterns across the Sierra Nevada, associated with the mesoscale winds, Sierra-Barrier-Jets (SBJ), North-Pacific-High (NPH), and long-range cross-Pacific westerlies, respectively. We find that dust emitted from the Central Valley is persistently transported eastward, while dust from the Mojave Desert and Great Basin influences the Sierra Nevada during mesoscale transport occurring mostly in the winter and early spring. Asian dust reaching the mountain range comes either from the west through straight isobars (cross-Pacific transport) or from the north in the presence of the NPH. Extensive dust depositions are found on the west slope of the mountain, contributed by Central Valley emissions and cross-Pacific remote transport. Especially, the SBJ-related transport produces deposition through landfalling atmospheric rivers, whose frequency might increase in a warming climate.

## 1. Introduction

The emission, transport, and deposition of mineral dust (hereafter dust) are processes receiving increasing interest from the scientific community (Sarangi et al., 2020). Dust emission is an integral part of aridification and mirrors the effects of climatic change and anthropogenic land use on global drylands (Duniway et al., 2019). Airborne dust interacts with Earth's climate system by altering radiation budget and cloud lifetime and amount (Forster et al., 2007; Haywood et al., 2005; Huang et al., 2019). Research has indicated that exposure to dust particles can cause respiratory infections, heart disease, and chronic obstructive pulmonary disease (COPD) (Laden et al., 2006; Lim et al., 2012; Crooks et al., 2016). A significant association between dust exposure and increased mortality has been reported, but there is no consensus in this regard to date (Giannadaki et al., 2014). The deposition of dust on snow surface influences snow albedo, further contributing to anthropogenic climate change as early as the 1970s (Qian et al., 2009; Qian et al., 2014; Skiles et al., 2018).

Dust over the southwestern U.S., particularly in California and Nevada states, is an important aerosol type contributing to more than half of surface aerosol concentrations in spring (Kim et al., 2021). Covered by dry soil with large gaps and sparse vegetation, the surrounding Mojave Desert, Sonoran Desert, and Great basin are susceptible to wind erosion (Okin et al., 2006; Duniway et al., 2019). The dry or ephemeral lakes in the deserts produce very fine dust containing toxic inorganic constituents (Goldstein et al., 2017). In addition, anthropogenic land-use practices – e.g., agriculture and human settlement, have greatly disturbed crustal biomass and produced windblown dust along the west coast (Pappagianis and Einstein, 1978; Clausnitzer and Singer, 2000; Neff et al., 2008). Furthermore, cross-Pacific dust transported from Asia and Africa to the Sierra Nevada range is widely reported (Ault et al., 2011; Creamean et al., 2014; Creamean et al., 2013). The surface dust concentration has been found to increase in the past two decades during spring at sites across the Southwest (Tong et al., 2017; Hand et al., 2017; Brahney et al., 2013), and the onset of dust season is shifting earlier in response to climate change (Hand et al., 2016). The elevated dust emission and earlier dust season are supposed to lead to a spectrum of environmental and societal

58    impacts in the most populated U.S. state. Especially, the resultant dust deposition on mountain snow

59    decreases snow albedo and produces a radiation forcing of 0-14.6 W m$^{-2}$ during the melting season (Huang

60    et al., 2022a), shifting snowmelt timing to earlier dates and further increasing California's vulnerability to

61    water resource fluctuations (Wu et al., 2018; Huang et al., 2022b). With its complex terrains, frequently

62    varying microclimate, and coexisting sources from both local and remote regions, the Sierra Nevada area

63    is an interesting region for studying dust transport and its response to climate change.

64    Characterization of dust emission, transport, and deposition across the Sierra Nevada has been

65    investigated using various data. Isotopic analyses (i.e., concentrations of Pb, Nd) are widely used to

66    distinguish and quantify the respective contribution of dust emission from local (dried Owen Lakes),

67    regional (Central Valley and the Mojave Desert), and global sources (Asia and Africa) on the dust

68    deposition on the mountain (Muhs et al., 2007; Jardine et al., 2021; Aciego et al., 2017; Aarons et al., 2019).

69    Their source attribution has been generally confirmed by the analyses of dust particle size and composition

70    (Creamean et al., 2014; Creamean et al., 2013; Reheis and Kihl, 1995). The isotopic and composition

71    analyses have been commonly used with back-trajectory modeling to further identify the dust transport

72    pathway from the source to the deposition location (Vicars and Sickman, 2011; Creamean et al., 2014;

73    Creamean et al., 2013). Yet, these analyses generally retrieve dust sources in a short time and at a specific

74    location. Alternatively, ground-based measurement networks were established in the 1990s and provide

75    long-term trends of dust concentrations and the interannual variability across multiple sites (Hand et al.,

76    2017; Achakulwisut et al., 2017; Hand et al., 2016). However, they do not contain information on dust

77    origins and atmospheric conditions responsible for dust transport. Satellite retrievals were less commonly

78    used to study dust characteristics across the Sierra Nevada (Lei and Wang, 2014), mainly due to the poor

79    data coverage caused by cloud contamination in the region.

80    Global and regional climate-chemistry models have been widely used to understand the drives of

81    the variability of dust and quantify the role of regional and remote transport, filling the gaps in the

82    observations (Chin et al., 2002; Chin et al., 2007; Kim et al., 2021; Wu et al., 2017). While dust emissions

83    and transport have been generally studied, there lacks a connection between dust emissions from the source

84  region and the timing, location, and amount of dust deposition to the Sierra Nevada snow. The isotopic and

85  composition analyses attribute dust sources at a few sites. But to our knowledge, no regional

86  characterization has been conducted on how dust is transported to the Sierra Nevada after emissions from

87  adjacent drylands and remote continents and when, where, and how much depositions occur for dust

88  transported through different pathways. The connection between dust emissions, transport pathways, and

89  deposition to snow would facilitate the prediction of future changes in dust regimes and the corresponding

90  climate impact, enabling more efficient management practices. With a focus on the dust that influences the

91  Sierra Nevada, this study investigates 1) Where does the dust come from? 2) How is dust transported to the

92  mountain from the sources? 3) How is the dust deposited on the Sierra Nevada during spring, when the

93  dust-in-snow largely influences snow albedo and snowmelt? We integrate models and observations to

94  understand how the dust deposition is linked to a specific source both surrounding and far from the Sierra

95  Nevada.

96

97  **2.1 Model and Reanalysis datasets**

98  **2.1.1 WRF-Chem configuration**

99  Table 1. Model configuration.

| Atmospheric processes | WRF-Chem Configuration |
| --- | --- |
| Meteorological IC/LBCs | ERA5 |
| Microphysics | Morrison double-moment |
| Radiation | RRTMG for both shortwave/longwave |
| Land surface | CLM4 with SNICAR |
| Surface layer | Revised MM5 Monin-Obukhov |
| Planetary boundary layer | YSU scheme |
| Cumulus | Grell-Freitas |
| Chemical driver | MOZART |
| Aerosol driver | MOSAIC 4-bin |
| Anthropogenic emission | NEI2017 |
| Biogenic emission | MEGAN |
| Biomass burning emission | FINNv2.2 |

| Dust emission | GOCART |
|---|---|
| Chemical IC/BC conditions | CAM-Chem |

100

101       We used the WRF-Chem version 3.9 to study dust emission and transport across the Sierra Nevada.

102 The model setups (Table 1), including the physical schemes and emission inventory, follow Huang et al.

103 (2022a), which showed that the model captures the distribution and variation in aerosols reasonably well in

104 the study domain (126.12-112.86°W, 32.3-43.0°N). The Model of Ozone and Related chemical Tracers

105 (MOZART) chemistry module (Emmons et al., 2020) and the Model for Simulating Aerosol Interactions

106 and Chemistry with four bins (MOSAIC 4-bin) aerosol model (Zaveri and Peters, 1999) were applied, and

107 dust emissions were calculated "online" using the GOCART dust scheme (Ginoux et al., 2001). The

108 meteorological initial and lateral boundary conditions were derived from the ECMWF Reanalysis v5

109 (ERA5) at 0.25° horizontal resolution and 6 h temporal intervals (Hersbach et al., 2020). Spectral nudging

110 was employed with a timescale of 6 h above the PBL to reduce the drift between ERA5 reanalysis data and

111 WRF's internal tendencies (Von Storch et al., 2000). The chemical initial and boundary conditions were

112 provided by CAM-Chem (Buchholz et al., 2019).

113       We applied the model to two nested domains (Fig. 1). Domain 1 (126.12-112.86°W, 32.3-43.0°N)

114 was configured to cover all of California, Nevada, and part of the surrounding states with $110 \times 120$ grid

115 cells at 10 km $\times$ 10 km horizontal resolution; the nested domain 2 covered the Sierra Nevada and

116 surrounding regions with a 2 km $\times$ 2 km resolution. The cumulus scheme is turned off in domain 2 with

117 convection-permitting resolution. We used 35 vertical model layers from the surface to 10 hPa with denser

118 layers at lower altitudes to resolve the PBL. The simulation period ranged from September 20, 2018, to

119 August 31, 2019 while we only used output from February to June in consideration of both dust emission

120 season and mountain snow existence (Hand et al., 2016; Kim et al., 2021; Achakulwisut et al., 2017).

Figure 1 WRF-Chem simulation domain 1 (D01) and domain 2 (D02) used in this study

**2.1.2 MERRA-2 and ERA5 reanalysis**

The Modern-Era Retrospective analysis for Research and Applications, Version 2 (MERRA-2) is a widely used atmospheric reanalysis with a spatial resolution of 0.500°×0.625° and 72 vertical layers (Buchard et al., 2017). MERRA-2 aerosol products are produced by combining GEOS atmospheric model version 5 (GEOS-5) with a 3D variational data assimilation algorithm to incorporate satellite observations, including Advanced Very High Resolution Radiometer (AVHRR), Moderate Resolution Imaging Spectroradiometer (MODIS), and Multi-angle Imaging Spectro Radiometer (MISR), as well as ground-based observations such as the AEronet RObotic NETwork (AERONET) (Gelaro et al., 2017). Although the aerosol vertical profile, composition, and size distributions are not constrained by the assimilation of aerosol optical depth (AOD), previous studies demonstrated that the aerosol assimilation system has considerably improved the agreement with numerous observed aerosol properties (Buchard et al., 2016; Buchard et al., 2017; Randles et al., 2017). The assimilation results in the imbalance of global dust mass and produces a considerably larger deposition than the simulated dust emission (Buchard et al., 2017).

137  MERRA-2 simulates dust with diameter bins of 0.2–2.0 (DU001), 2.0–3.6 (DU002), 3.6–6.0 (DU003), 6.0–

138  12.0 (DU004), and 12.0–20.0 (DU005) μm, while the MOSAIC 4-bin in WRF-Chem simulates dust with

139  geometric size bins of 0.039–0.156, 0.156–0.625, 0.625–2.5, and 2.5–10.0 μm. We therefore use the dust

140  concentrations of the first 4 size bins in MERRA-2 (DU001 + DU002 + DU003 + 0.74 * DU004) to match

141  with      dust      with      geometric      size      less      than      10.0      μm      in      WRF-Chem

142  (https://gmao.gsfc.nasa.gov/reanalysis/MERRA-2/FAQ/).

143       ERA5 provides assimilated wind fields at a 0.25°×0.25° horizontal resolution at 137 hybrid

144  sigma/pressure levels from 1979 to near real time (Hersbach et al., 2020). This study obtained the 3-hourly

145  meridional and zonal wind field from February to June 2019 from 1000 to 500 hPa. The ERA5 wind

146  reanalyses were used with satellite-retrieved dust optical depth (DOD) to evaluate the classified dust

147  emission and transport patterns from the model.

148

149  **2.2 Satellite observations for validation**

150       The Infrared Atmospheric Sounding Interferometer (IASI) onboarded European Meteorological

151  Operation (MetOp) satellite series measures infrared radiation in 8,461 spectral channels between 3.63 and

152  15.5 μm. The instrument provides near-global coverage with a spatial resolution of 12 km at nadir (Hilton

153  et al., 2012) since 2007. IASI is primarily sensitive to coarse mode dust particles, and thus the retrieved

154  AOD at the wavelength of 10 μm can represent the DOD (Yu et al., 2019). Note that the thermal infrared

155  (IR) AOD reported by IASI is usually significantly smaller than the visible AOD in MODIS, because of

156  the spectral dependence of dust extinction (Zheng et al., 2022). We use the version 2.2 AOD product

157  developed at the Centre National de la Recherche Scientifique Laboratoire de Météorologie Dynamique

158  from https://iasi.aeris-data.fr/dust-aod/ (February 2022) (Capelle et al., 2014). The 0.3°×0.3° daily AOD

159  data covering California were produced by aggregating day and night retrievals at the satellite pixel

160  resolution (Capelle et al., 2018), in consideration of both data completeness and fine features. The 1.0°×1.0°

161  daily AOD was produced in a similar way to investigate dust transport from Asia across the North Pacific.

162  The MIDAS (ModIs Dust AeroSol) dataset provides global fine-resolution (0.1°×0.1°) daily DOD

163  between 2003 and 2017 using quality-filtered AOD from MODIS Aqua and DOD-to-AOD ratios from

164  MERRA-2 reanalyses (Gkikas et al., 2021). Despite the uncertainties in modeled DOD-to-AOD ratios, the

165  validations of the MIDAS dataset against the AERONET dust-like AOD and the LIdar climatology of

166  Vertical Aerosol Structure for space-based lidar simulation (LIVAS) DOD reveal a high level of agreement

167  at both global and station level (Gkikas et al., 2022). Compared with other MODIS-derived DOD products

168  (Song et al., 2021; Voss and Evan, 2020; Ginoux et al., 2012; Pu and Ginoux, 2018), MIDAS has finer

169  spatial and temporal resolutions over both land and ocean, which is particularly applicable in this study

170  focusing on a small region and a few cases at daily scale. The dataset has been extended to near real-time

171  to match our study year.

172  Cloud-Aerosol Lidar with Orthogonal Polarization (CALIOP) is a two-wavelength (532 and 1064

173  nm) polarization lidar onboarded the Cloud-Aerosol Lidar and Infrared Pathfinder Satellite Observation

174  (CALIPSO) satellite (Hunt et al., 2009). Since June 2006, the lidar has been collecting an almost continuous

175  record of high-resolution profiles of aerosol and clouds as fine as 30 m in the vertical, covering 82°N to

176  82°S (Winker et al., 2010; Winker et al., 2009). This study used clear-sky data from the CALIOP Version

177  4, level-2 aerosol profile product (Young et al., 2018) to investigate the vertical profile of elevated dust

178  layer, especially from remote transport. When there were large DOD shown in IASI and MIDAS, we

179  examined the vertical profiles of dust by identifying the "dust," "polluted dust," and "dusty marine" species

180  in the CALIOP data (Kim et al., 2018)

181

182  **2.3  SOM analysis**

183  We applied the self-organizing map (SOM), a clustering method developed in the field of artificial

184  neural networks, to recognize different weather features associated with dust transport and deposition.

185  SOM has been widely used in atmospheric sciences to recognize spatially organized sets of patterns in the

186  data (Reusch et al., 2007; Bao and Wallace, 2015; Liu et al., 2022; Song et al., 2019). Before the machine-

187  learning process, Before the machine-learning process, we assign a few two-dimensional arrays of initial

188 nodes randomly or more efficiently from the leading empirical orthogonal functions (EOFs). During the

189 training phase, the Euclidean distance between each input pattern and the initiation nodes is calculated to

190 begin an iterative procedure. The best-matching node or the "winning" node is the one with the smallest

191 distance between the initiation nodes and the input vector. Then the winning node and the neighborhood

192 nodes around the winner are updated to adjust themselves toward the input vector. Since this process is

193 iterated and fine-tuned, the nodes are self-organizing. The final SOM nodes represent typical dust transport

194 and deposition patterns across the Sierra Nevada.

195 Here, we first used five variables from WRF-Chem inner domain (D02) in the SOM clustering,

196 including dust deposition flux at the Sierra Nevada, the low-level meridional and zonal dust transport fluxes,

197 and the mid-level meridional and zonal dust transport fluxes surrounding the Sierra Nevada. The original

198 fields were used without any no filtering methods to consider the extreme cases. The 3 hourly model outputs

199 during February-June 2019 are used to count for the spatial distribution and temporal evolution of dust

200 transport and deposition. For WRF-Chem, we averaged the zonal and meridional dust fluxes in model levels

201 3-5 (roughly 900-950 hPa over coastal California and 650-700 hPa over the Sierra Nevada) to acquire the

202 low-level transport features. We averaged 200-700 hPa fluxes to acquire the mid-level transport features.

203 Levels 3-5 were selected to focus on airborne particulate matter entrained above the planetary boundary

204 layer and transported on the regional scale. Remote transport of Asian and African dust is mostly found

205 around 600–200 hPa, which flows downward to the lower troposphere along the post-cold isentropic surface

206 into the atmospheric river (AR) environment (Voss et al., 2021). By selecting levels between 200-700 hPa,

207 we were able to include all cross-Pacific remote transport in the middle level.

208 We tested the number of clusters ($k$) that ranges in 3, 4, 5, 6, 8, 9, and 16 to assess the distinctiveness

209 and robustness of different $k$. For each $k$, the robustness of the clusters was measured by a classifiability

210 index (CI) (Vigaud and Robertson, 2017; Vigaud et al., 2018; Hannachi, 2010) constructed using the

211 minimum spatial correlation coefficient between the clusters obtained from the full data and many random

212 halves of the data (100 halves used here) (Hannachi, 2010). Therefore, the CI measured the reproductivity

213 of the $k$ clusters partitioning (Visbeck et al., 2001), with perfect partitioning leading to 1. Figure S1 shows

214 the CI as a function of the number of clusters using WRF-Chem output for 2019. With the highest CI, the

215 4-cluster partitioning well represents distinct dust transport and deposition patterns over the Sierra Nevada

216 and is used in this study.

217        To verify the recognized transport patterns based on WRF-Chem, we conducted SOM analyses

218 using variables from MERRA-2. We first remapped the same five variables using bilinear interpolation

219 from $0.5° \times 0.625°$ to 10 km, the resolution of the WRF-Chem outer domain, before clustering. The vertical

220 levels of low-level and mid-level dust transport fluxes were selected to approximately match the WRF-

221 Chem pressure level. Four nodes were identified and arranged to make a direct comparison with those from

222 WRF-Chem. To further investigate if transport patterns recognized from SOM vary significantly with years,

223 we applied SOM analyses over 2001-2021 using MERRA-2 extended records of dust fluxes and

224 deposition.

225

226 **3. Results**

227 **3.1 Dust emission sources around the Sierra Nevada**

228        We find four emission source regions surrounding the Sierra Nevada where dust emissions could

229 potentially influence the mountain snow impurities between February and June (Fig. 2). The Mojave Desert,

230 located southeast of the Sierra Nevada, is characterized by low annual precipitation, sparse vegetation, and

231 dried fine soil. Airborne dust loading over the desert can reach 30000 ug m$^{-2}$ averaged over our study period

232 (Fig. 2a). It is generally transported eastward but can also be transported westward, influencing the southern

233 part of the mountain (Neff et al., 2008). Dust produced in the northern (Sacramento Valley) and the southern

234 part (San Joaquin and Tulare Basins) of the Central Valley is often transported eastward to the mountains.

235 With high soil aridity and a higher fraction of dry sand (Duniway et al., 2019), the southern Central Valley

236 is more erodible and emits a higher amount of fine dust. The Great Basin dust is relatively weak in

237 magnitude but located at a higher altitude. Therefore, it can easily ride along wind currents upward along

238 the east slope of the mountain. The column dust loading in MERRA-2 confirms our results in WRF-Chem

239 (Fig. 2b), despite it showing a stronger dust emission in the Great Basin while a weaker one in the

Sacramento Valley. The IASI shows the strongest IR DOD in the Mojave Desert, followed by the southern

Central Valley, but smaller dust emissions from the Sacramento Valley as compared with model output

(Fig. 2c). The smaller magnitude is largely due to the fact that IASI measures the radiation at IR

wavelengths, which is more sensitive to coarse-mode dust particles (Yu et al., 2019), whereas the fine dust

produced in the Central Valley has a negligible contribution to DOD at 10 μm. In contrast, MIDAS captures

dust emissions from the Great Basin, the southern and northern Central Valley (Fig. 2d) but not the Mojave

Desert. MIDAS is reported to underestimate DOD from the Mojave Desert compared to AERONET DOD,

which might be caused by the lower dust amounts simulated in MERRA-2 (Gkikas et al., 2021) and the

underestimation of MODIS AOD over the deserts as compared to ground observations (Tao et al., 2017).
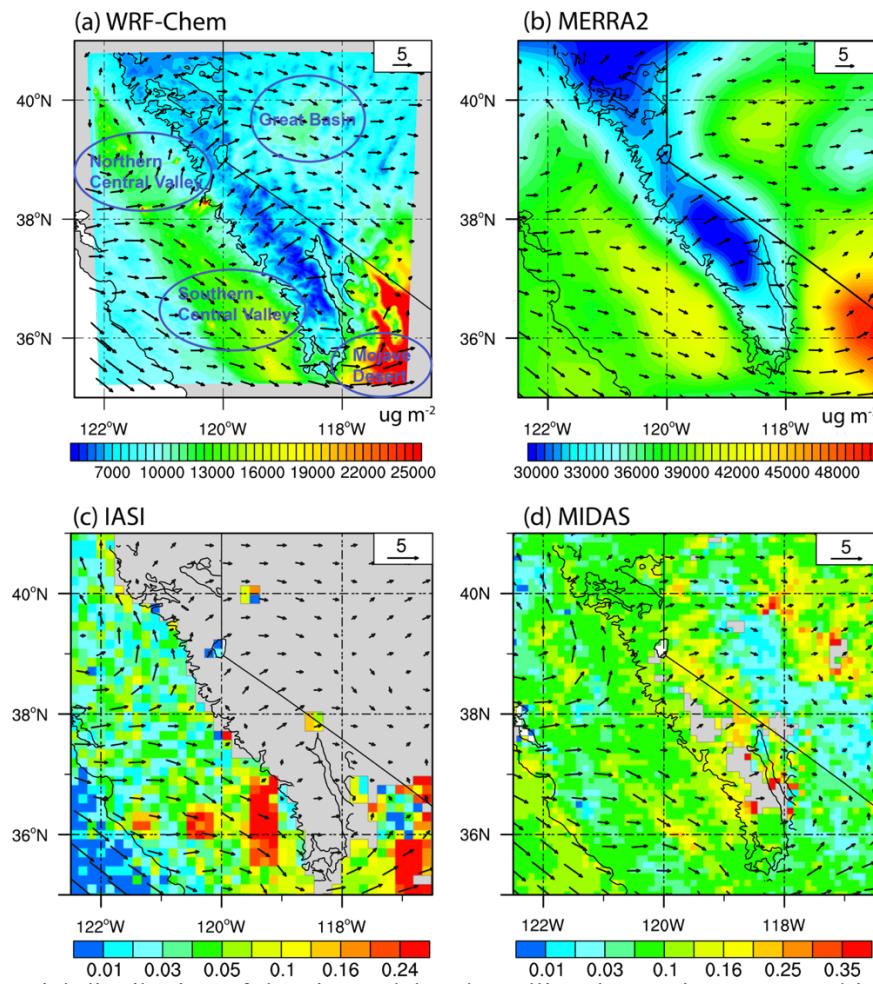
**Figure 2** The spatial distribution of dust in model and satellite observations averaged in 2019 February-June. Column dust loading (ug m$^{-2}$) and low-level winds (roughly 875-925 hPa; m s$^{-1}$) in (a) WRF-Chem and (b) MERRA-2. (c) Observed thermal infrared DOD at the wavelength of 10 μm from IASI (d) Observed visible DOD at the wavelength of 550 μm from MIDAS. The low-level winds (m s$^{-1}$) in (c) and (d) are from

254 ERA5 reanalyses. Black contours indicate the elevation of 1500 m, which represents the Sierra Nevada
255 range used in this study. The grey area in c-d are missing pixels in satellite observations
256

## 3.2 Dust transport across the Sierra Nevada
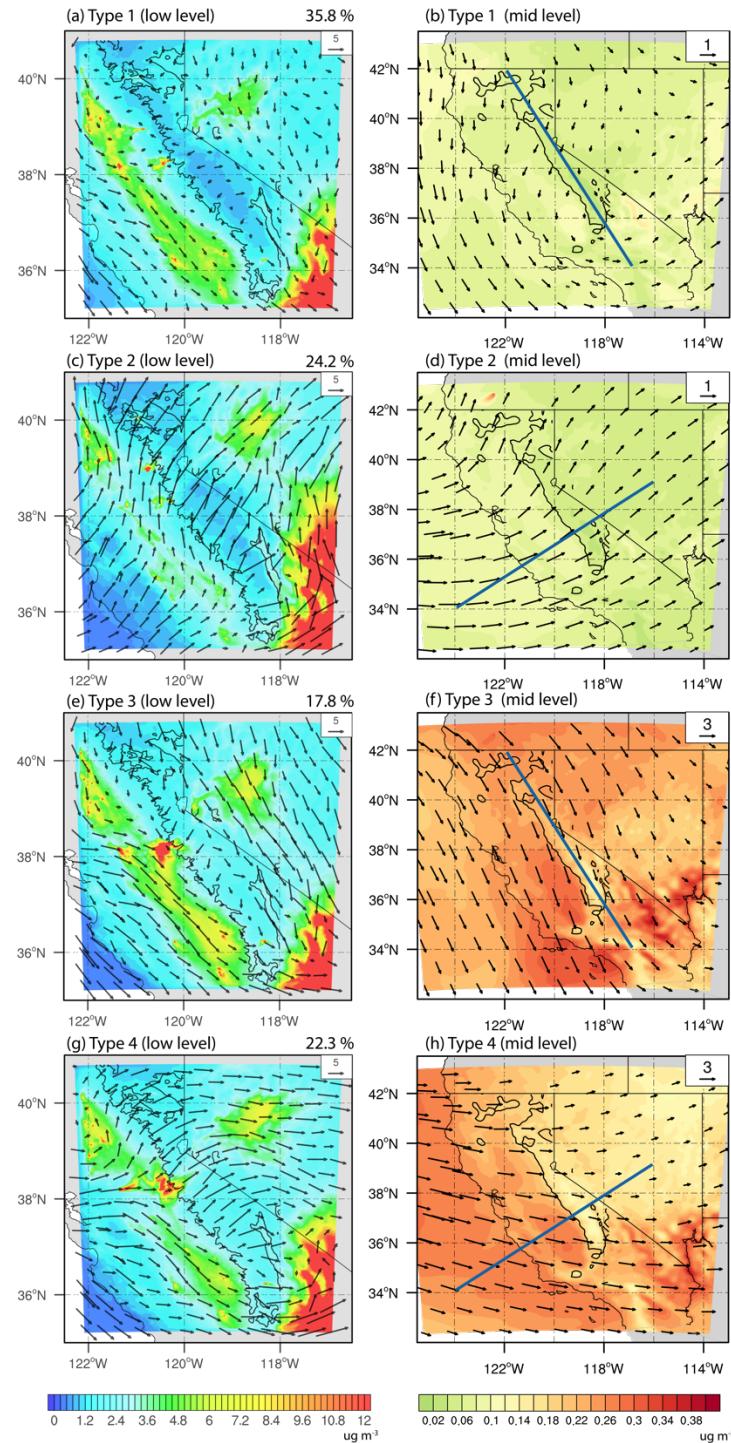
258
259 **Figure 3** (a, c, e, g) Low-level (roughly 875-925 hPa) dust concentration (ug m$^{-3}$) and wind vectors (m s$^{-1}$)
260 in each of the four SOM type in WRF-Chem; The numbers on the top right of subplots denote the frequency

261  of each type. (b, d, f, h) Mid-level (200-700 hPa average) dust concentration (ug m$^{-3}$) and dust transport in
262  types 1-4; The position of the cross-section used for Figure 5 is denoted in each plot.
263

264       This section introduces the features of dust transport patterns discerned from WRF-Chem and

265  evaluates them against satellite observations over the period of February to June 2019. Figure 3 shows the

266  WRF-Chem dust concentration and wind in the low levels and middle levels averaged for each of the four

267  types acquired from the SOM analyses. The dust transport pattern represented in SOM type 1 accounts for

268  35.8% of hours from February to June (Fig. 3a), especially in February (43%) and March (57%) (Fig. 4a).

269  Type 2 occurs in 24.2% of the whole study period and contributes to more than 50% in February and then

270  decreases with the month. In contrast, types 3 and 4 account for 17.8% and 22.3%, respectively, with the

271  occurrence increasing with the month. The maximum occurrence is found in June for type 3 (40%) and

272  April for type 4 (34%), respectively.

273  **3.2.1 Mesoscale regional (MSR) transport**
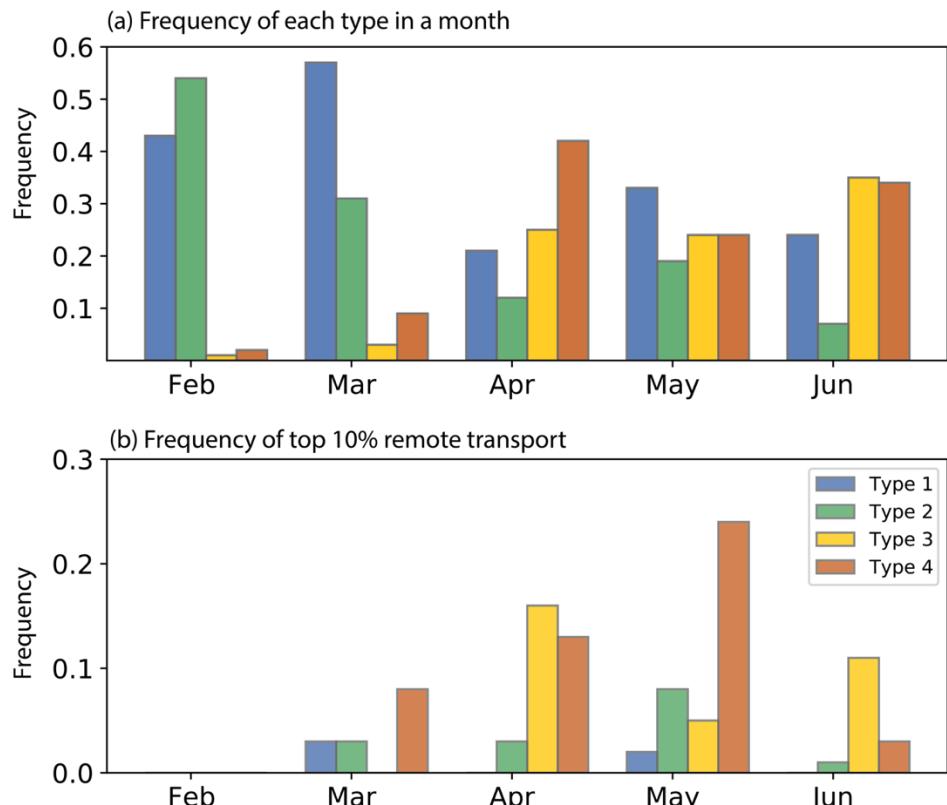
274
275  **Figure 4** (a) The frequency of each type (the time dominated by each type divided by total time in a month)
276  that occurs in February, March, April, May, and June in WRF-Chem. (b) The frequency of each type in the

277 top 10% remote transport (the time dominated by each type divided by total time of the top 10% remote
278 transport).
279

280    In type 1, dust is transported from northwest to southeast in the Central Valley in the low level

281 (roughly 875-925 hPa over the California coast). A vortex (Schultz Eddy) was found in the northern Central

282 Valley (Fig. 3a), circulating counter-clockwise and confining dust to the local environment (Bao et al.,

283 2008). The air inflow from the ocean is relatively weak and obstructed by the terrain. The Great Basin is

284 dominated by the northwesterlies. The emitted dust is transported southeastward and blocked by the

285 mountain, depositing dust on the east slope. Dust emitted from the Mojave Desert can be elevated to the

286 middle level (Fig. 3b). The cross-section further shows a vertical circulation where the Mojave Desert dust

287 is blown away from the Sierra Nevada at the low level and towards the mountain at 600-700 hPa (Fig. 56a).

288 A weaker mid-level cross-Pacific flow is found in type 1 than in other types (Fig. 65a), with no signals of

289 remote transport reaching the Sierra Nevada (Fig. 3b). Type 1 generally corresponds to the dust transport

290 in lack of prevailing large-scale weather systems. The high peaks of the Sierra Nevada produce mesoscale

291 circulations and prevent the Central Valley and Great Basin dust from being transported to the other side

292 of the mountain. It is referred to as the "mesoscale regional (MSR) transport" hereafter.
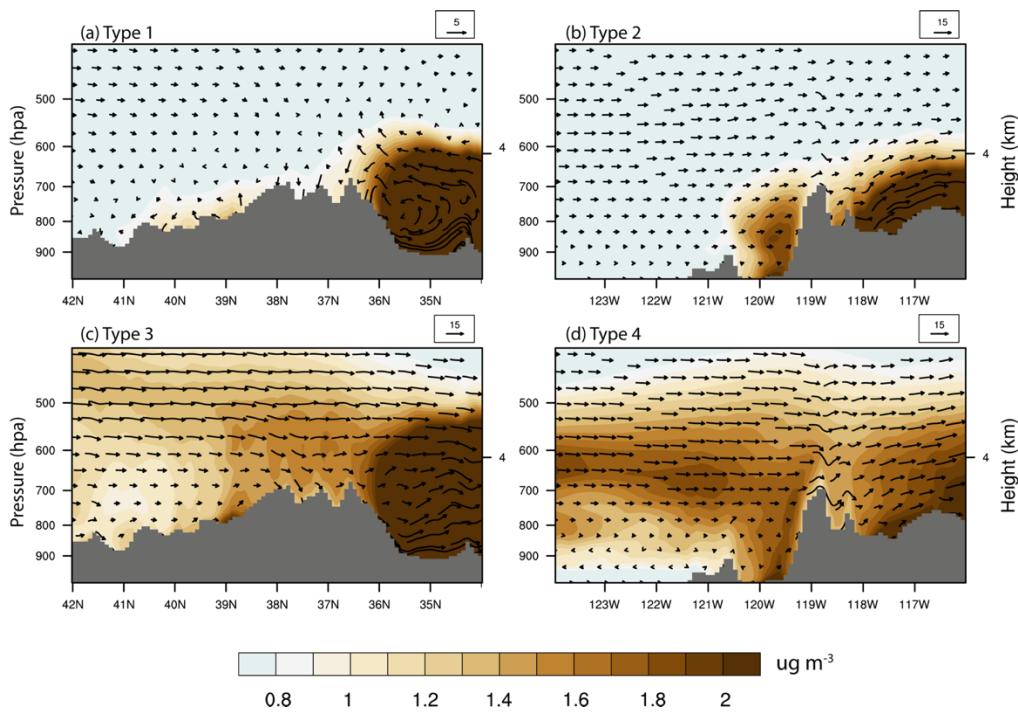
293

294 **Figure 5** Cross-section of dust concentration (shaded; ug m$^{-3}$) and dust transport fluxes (vectors; ug m$^{-2}$ s$^{-1}$) at 1000-400 hPa for each SOM type in WRF-Chem. The position of each cross-section is denoted in Fig. 3 b (Type 1), d (Type 2), f (Type 3), and h (Type 4). The grey area indicates the topography of the Sierra Nevada.
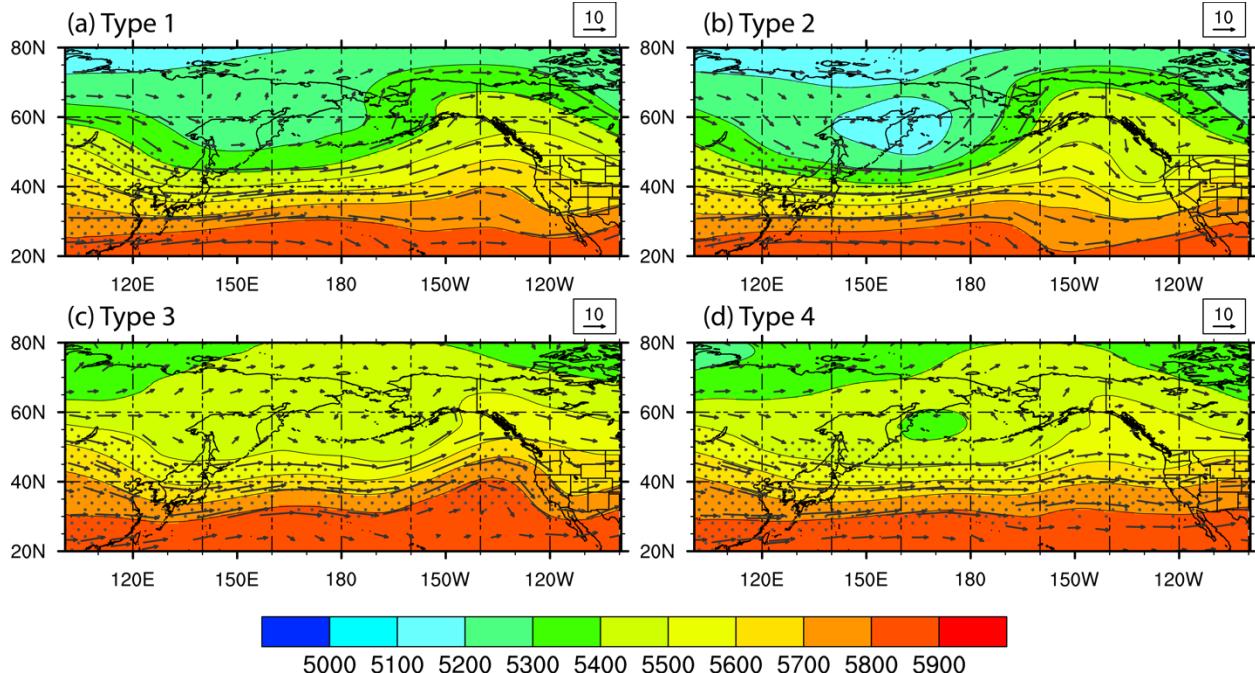
298

299 **Figure 6** Geopotential height (gpm) and wind vectors (m s$^{-1}$) at 500 hPa in each of the four SOM types in WRF-Chem. The dotted regions indicate DOD higher than 0.03 from MERRA-2

301

302       We validate the features of type 1 from WRF-Chem using satellite retrieved DOD and wind vectors

303 from ERA5. The cloud contamination results in many missing satellite pixels in our study domain, making

304 the transport patterns hard to discern on a single day. DOD and winds belonging to the same SOM type on

305 consecutive days are averaged to maximize the data completeness. One typical example for each type is

306 presented based on their representativeness and the maximum spatial coverage. Figures 7a-b present dust

307 emission and transport patterns during May 10-12, a typical case for the MSR transport. In IASI, we find

308 peak IR DOD (> 0.2) over the Mojave Desert and the southern Central Valley and moderate values in the

309 Sacramento Basin related to the Schultz Eddy (Fig. 56a), resembling the relative magnitude of dust

310 concentrations in regional source regions in WRF-Chem (Fig. 3a). MIDAS shows another evidence of dust

311 transport pathways within the Central Valley with a higher resolution, although the maximum DOD shifts

312 slightly towards the mountain range (Fig. 7b). Dust emissions from the Great Basin are weaker than those

313 from the southern Central Valley.

314
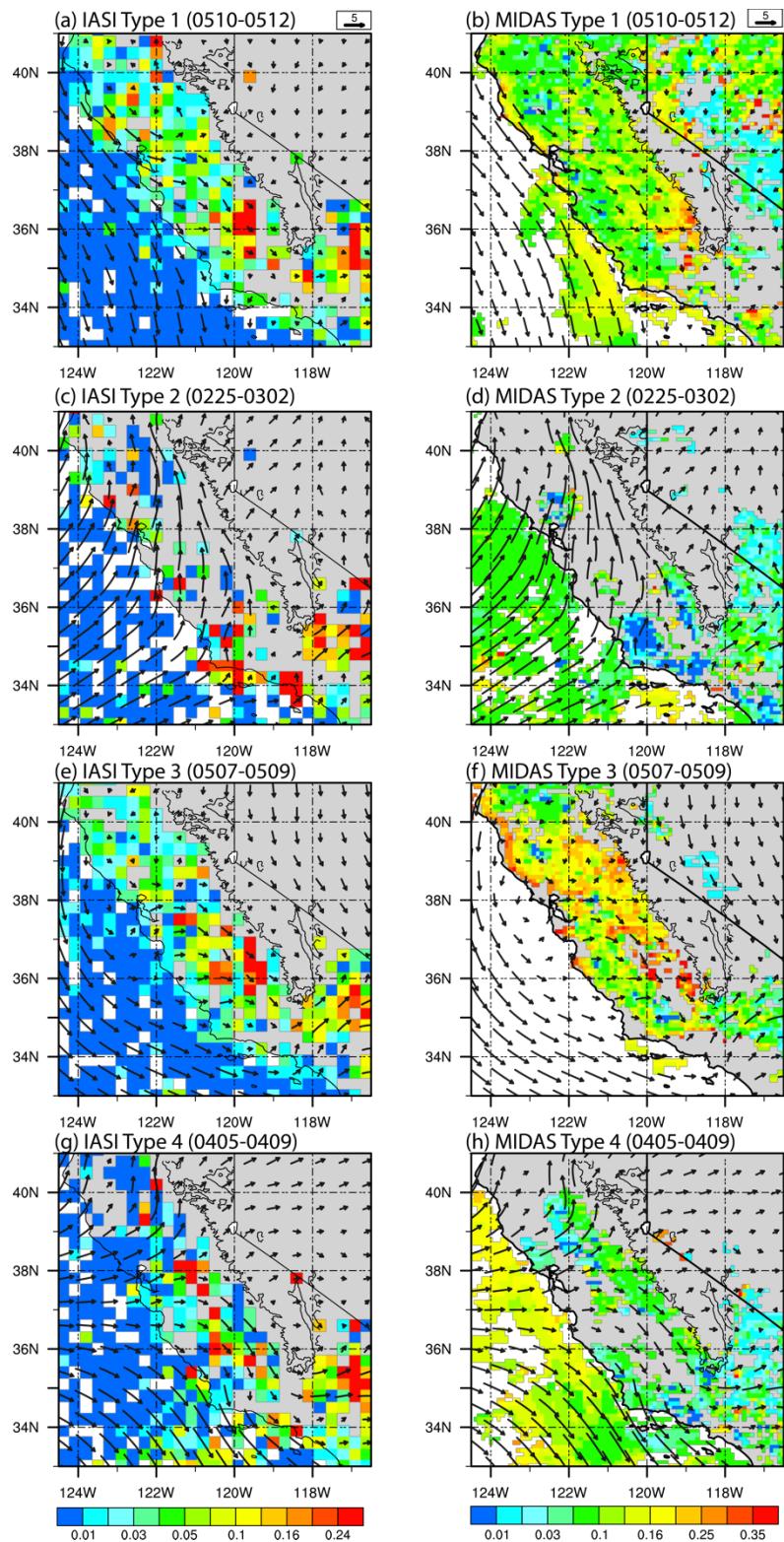
**Figure 7** (a,c,e,g) IR DOD at the wavelength of 10 μm retrieved from IASI and (b,d,f,h) visible DOD at the wavelength of 550 μm from MIDAS for each type. The low-level winds (vectors; m s$^{-1}$) are obtained from the ERA5 reanalyses. The numbers in the parenthesis indicate the event time period for the year 2019.

### 3.2.2 Sierra-barrier-jets-related (SBJ-related) transport

In type 2, the low-level winds turn to the north above the western slope of the Sierra Nevada (Fig. 3c), which resembles the terrain-locked Sierra barrier jets (SBJs) typically observed during the presence of ARs (Neiman et al., 2013). The large-scale pattern consists of a low 500hPa geopotential height (GPH) center in the north Pacific (Fig. 65b). The meridional gradient produces intense storm tracks from Kuroshio Current towards Alaska (Rodionov et al., 2007). Indeed, we find extensive precipitations in type 2 (not shown), which produce more wet deposition along the mountain's windward (west and south-facing) slopes and result in cleaner air in the Central Valley (Fig. 3c). The dust layer at the Central Valley is found below 700 hPa, mostly blocked by the high mountain peaks and is hardly transported to the lee-side (east) slope of the mountain (Fig. 56b), despite the cross-barrier westerlies found in the middle level. Dominated by SBJs, dust generated in the Great Basin and the Mojave Desert is blown away from the mountain. No clear signal of remote transport is found on the California coast (Fig. 3d). The dust transport from all sources is closely connected to SBJ; therefore, type 2 is referred to as the "SBJ-related" transport. In both IASI and MIDAS, we find more missing pixels for SBJ-related transport than any other type caused by cloud contamination (Figs. 7c-d). The AR-related landfalling precipitations from February 25 to March 2 remove the airborne dust particles. A cleaner atmosphere might be induced, but it is hard to confirm considering the missing pixels over the continent.

### 3.2.3 North-Pacific-High-related (NPH-related) transport

Type 3 has northwestern winds in both Central Valley and the Great Basin (Fig. 3e), transporting Central Valley dust to the southwest part of the Sierra Nevada in early summer. It is known as the "North-Pacific-High-related (NPH-related)" transport, during which the North Pacific High (NPH) built up in the north Pacific 130° W produces the northwest-southeast wind direction along the California coast (Fig. 65c), influencing the transport patterns for dust emitted from the surrounding sources. At the middle level, we observe a meridional mid-level dust transport pathway (Fig. 3f), which appears at 400-500 hPa in the

343   northern Sierra Nevada and descends to 700 hPa at 36-37 °N, the top of the southern Sierra Nevada (Fig.

344   56c). "The MERRA-2 reanalysis DOD (Fig. 6c) further shows dust originating from Asia is transported

345   towards North America following the isobars and wind patterns (discussed further in section 3.2.3). The

346   dust emitted from the Great basin is transported by the southward winds to the east slope of the mountains,

347   while emissions from the Mojave Desert are transported away from the mountain range.

348   The simulated dust concentration and transport in the NPH-related transport are confirmed by DOD

349   observations during May 7-9, with the transport pathway parallel to the California coast (Figs. 7e-f). Studies

350   have shown two main pathways of Asian dust transport to North America during the spring months: (1)

351   meridional excursions north into Alaska and then south along the U.S. west coast, and (2) zonal transport

352   over the North Pacific Ocean (Creamean et al., 2014). With north-south dust transport at the middle level,

353   the NPH-related transport characterizes the first pathway. To examine this hypothesis, we averaged the IR

354   DOD and 500 hPa wind field over the North Pacific during May 2-9. We included a few days before the

355   event (Fig. 8a) as it takes 7-10 days for dust to be transported from Asia to North America (Ault et al., 2011;

356   Creamean et al., 2013). The dust transport pathway shows that after being emitted from East Asia and the

357   Gobi Desert, dust is transported zonally to 150 °W, excursing north into Alaska/Canada and then traveling

358   south along the U.S. west coast. Similar conclusions can be drawn with more evident pathways using DOD

359   from MERRA-2 reanalyses (Fig. 8e). An elevated dust belt from 8 km to 12 km is discerned over the North

360   American coast (27 °N to 60 °N) from the CALIOP data, denoting the north-south transport of a thin dust

361   layer through the middle level (Fig. 8c).
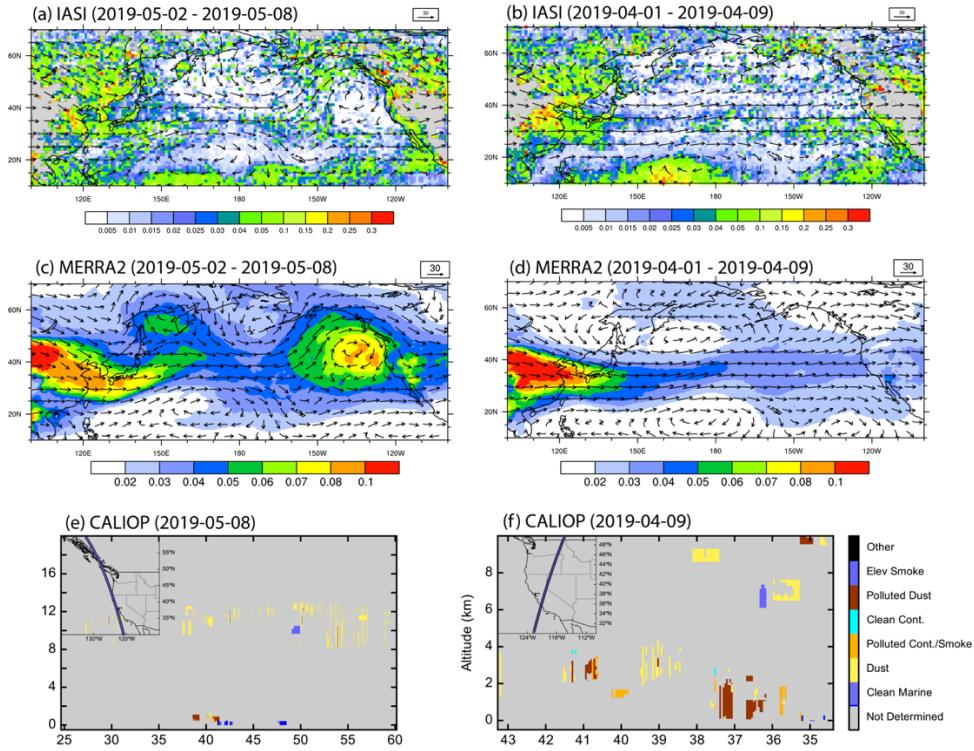
362
363 Figure 8 (a) IR DOD from IASI and 500 hPa winds (m s$^{-1}$) from ERA5 over the North Pacific for a typical
364 Type 3 case averaged between 2019-05-02 to 2019-05-08; (b) same as (a) but for a typical type 4 event
365 averaged between 2019-04-01 to 2019-04-09; (c) DOD from MERRA-2 and 500 hPa winds (m s$^{-1}$) from
366 ERA5 for a 3 event; (d) same as (c) but for a type 4 event; (e) latitude-height cross-section of aerosol species
367 from CALIOP on 2019-05-08 (Type 3); (f) same as (e) but for a typical Type 4 case on 2019-04-09

368

## 3.2.4 Cross-Pacific zonal (CPZ) transport

370     Air inflows from the ocean enter California and diverge to the northern and southern branches in

371 type 4, transporting dust eastward across the Sierra Nevada (Fig. 3g). At the middle level, the low-GPH

372 center recedes in April, and the isobars become straighter than in boreal winter, which facilitates the zonal

373 transport of dust emitted from middle Asia over the North Pacific Ocean (Fig. 65d). The cross-section

374 further shows an elevated dust layer is transported from the ocean at around 700-500 hPa (Fig. 56d). The

375 concentrations are much stronger, and the altitude also lower than the NPH-related transport (Fig. 56c). The

376 remotely transported dust descends to low altitudes when reaching the California coast and converges with

377 the dust from the Central Valley at around 800 hPa. A portion of dust is compacted to the windward slopes

378 at higher elevations, and the remaining across the mountains affects the east slope. Dust emitted from the

379   Great Basin and the Mojave Desert is transported away from the mountains. Type 4 is denoted with "cross-

380   Pacific zonal (CPZ) transport" to reflect the strong cross-Pacific dust transport.

381           April 5-9, a typical case for the CPZ transport, clearly shows the north and south branches of dust

382   transport over the Central Valley (Figs. 7g-h). Different from the NPH-related transport pathway, the large-

383   scale DOD and winds at 500 hPa (averaged over April 1-9) show that dust emitted from East Asia is being

384   transported eastward, with a belt of IR DOD > 0.1 evident around 25-40 °N (Fig. 8b). The DOD from

385   MERRA-2 confirms the zonal pathways of dust transport with a smaller magnitude (Fig. 8d). The vertical

386   distribution shows an elevated dust layer at 2-4 km above ground level, reaching the higher elevation of the

387   mountain (Fig. 8f).

388           We calculated the mid-level dust remote transport, defined as the dust influxes from the north and

389   west boundaries of the 200-700 hPa of WRF-Chem modeling domain 1, and investigated how the top 10%

390   largest remote transport distribute in each SOM (Fig. 4b). Among all the large remote transport, CPZ

391   transport accounts for 48% while NPH-related accounts for 32%, indicating that the zonal pathway plays a

392   more important role in the cross-Pacific transport. Most remote transports are found in April and May, the

393   former dominated by the meridional transport in the existence of the NPH while the latter led by the CPZ

394   transport. The remaining two types contribute to a fairly small portion consistent with the clean atmosphere

395   in the middle levels (Figs. 3b, d).

396

397   **3.2.5 Dust emissions and tranport in back trajectory analyses**

398           We discern four types of dust transport patterns across the Sierra Nevada using the SOM clustering

399   method. The MSR transport represents the local dust transport, which contributes to more than 20% of the

400   time each month during February-June (Fig. 4a) in the absence of prevailing weather systems. The SBJ-

401   related air inflows transport dust eastward and are closely related to the AR, during which the GPH and

402   storm tracks at 500 hPa feature a typical large-scale pattern during the boreal winter (Rodionov et al., 2007).

403   As time evolves, the GPH center recedes, and the isobars become more straight zonally in April, bringing

404   dust from Asia and Africa to the western U.S. coast (CPZ transport). In early summer, the buildup of NPH

in the east Pacific corresponds to north-south winds along the California coast, transporting dust along the

Sierra Nevada (NPH-related transport).

We further conducted air mass back trajectory (AMBT) simulations to evaluate the dust emission sources and transport pathways identified using SOM analyses. The back trajectory simulation was conducted using Hybrid Single-Particle Lagrangian Integrated Trajectory (HYSPLIT) model with meteorological forcings from North American Mesoscale Forecast System. We selected typical days for the four SOM types as in Figure 7 and three sites located at the Central Sierra Nevada (38 °N, 120.3°W), Southern Sierra Nevada (36.5 °N, 119 °W), and Eastern Sierra Nevada (37 °N, 117 °W), to represent dust deposition at different subregions.

The results of 12-hour and 7-day AMBT results corroborate the identified local and long-range transport pathways for each type. The transport pathways generally follow the wind directions shown in Figure 7. Multiple emission source regions are found in type 1, including the Central Valley where dust is transported eastward to the windward slopes and the Great Basin where dust is transported westward to the lee-side slopes (Fig. S2). In type 2, dust deposited in all three sites comes from the Central Valley (Fig. S2), and the transport corresponds to the direction of SBJ during AR (Fig. 7c). Types 3 and 4 are affected by both local and remote transport. Locally, Dust mainly comes from the northern California and the Great Basin in type 3, while it comes from the Central Valley in type 4. Remotely, in type 3, we find dust emitted from Asia and North Africa excurses meridionally to Alaska at 135° W and then travels southward along the U.S. West Coast (Fig. S3a). In contrast, dust emitted from east Asia is transported zonally across the Pacific, reaching the Sierra Nevada from the west (Fig. S3b).

## 3.3 Dust deposition over the Sierra Nevada

The averaged dust deposition and low-level dust transport for each type are shown in Fig. 9, including both dry and wet depositions. The dry depositions consider the diffusion and gravitational effects, while wet depositions describe in-cloud removal (rainout) and below-cloud removal (washout) by grid-resolved stratiform precipitation as well as the sub-grid wet scavenging (Chapman et al., 2009; Easter et al., 2004).

431 In all SOM types, extensive depositions are found on the west slope in all types, generally decreasing with

432 elevation.

433     The MSR transport has the smallest deposition among the four types (Fig. 9a). Large depositions are

434 found in the southern Sierra Nevada and Lake Tahoe. Dust contributing to the deposition origins mainly

435 from the Mojave Desert and the Great Basin dryland. In contrast, large depositions found in the southern

436 and eastern parts of the mountains in NPH-related transport may be produced in agricultural land from the

437 southern Central Valley, as we find a persistent eastward transport pathway in the low level (Fig. 9c). The

438 remote transported dust plays a minor role as it is located above 8 km in altitude.
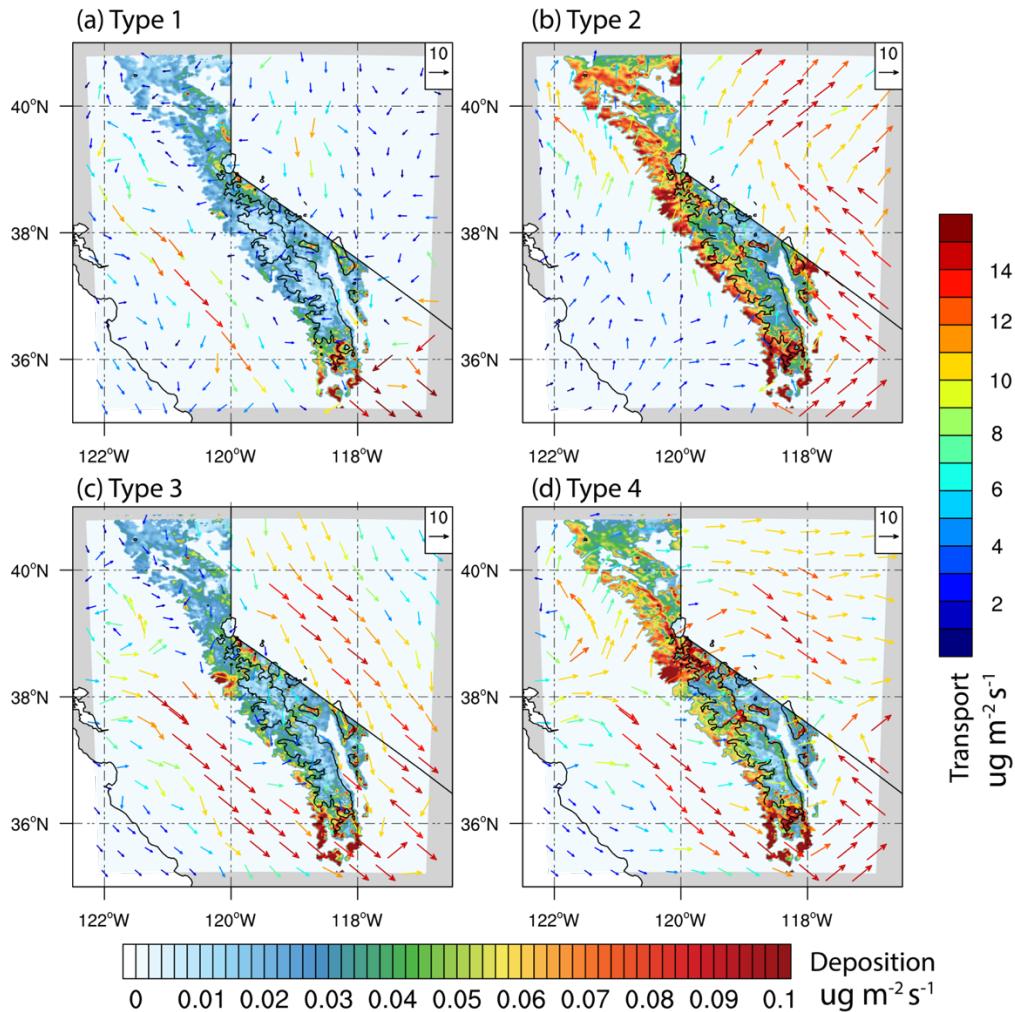
439
440 **Figure 9** (a-d) Dust deposition (shaded; ug m$^{-2}$ s$^{-1}$) over the Sierra Nevada and low-level dust transport
441 fluxes (colored vectors; ug m$^{-2}$ s$^{-1}$) across the Sierra Nevada averaged over each of the four SOM types in
442 WRF-Chem. Black contours indicate an elevation of 2500 m. The bottom color bar shows the magnitude
443 of dust deposition over the Sierra Nevada while the right color bar shows the magnitude of dust transport
444 flux vectors.

445

446     While SBJ-related transport has the lowest low-level dust concentration over the Central Valley, it

447     produces the largest deposition along the west slope (Fig. 9b). Most eastward transport in the southern

448     Sierra Nevada is obstructed by the high mountain peaks, resulting in large depositions below 2900 m. The

449     SBJ turns eastward in the Sacramento Basins and climbs through the mountain north of 38 °N, producing

450     a relatively homogenous deposition in the northern part. The combination of dust transport and deposition

451     indicates that dust influencing the mountain snow impurities mostly comes from the Central Valley.

452     Compared with the other SOM types, SBJ-related transport has large depositions at elevations higher than

453     2500 m (discuss later). Large depositions are also found in the CPZ transport (Fig. 9d), with the largest

454     value occurring on the west slope of the central and southern Sierra Nevada, contributed by both Asian dust

455     and Central Valley dust. Compared to the MSR and NPH-related transport, the large-scale westerlies in the

456     Central Valley (SBJ-related and cross-Pacific transport) produce larger deposition, probably because of the

457     more efficient removal of particles by collision with terrestrial surfaces at higher elevations (Fig. 56d).

458     To quantify the relative importance of wet and dry depositions in each 3 hourly total deposition data,

459     we calculate the fraction of wet depositions to total depositions averaged over the Sierra Nevada:

460     $\frac{Wet\ deposition}{Wet\ deposition+Dry\ deposition}$. The contribution of dry deposition is defined in a similar way. We find the

461     wet deposition accounting for 40% in frequency in the SBJ-related type. The landfalling precipitation has

462     deposited large amounts of airborne dust on the snow surface, producing a cleaner atmosphere as we have

463     found in Fig. 3c. The frequent wet depositions also explain the larger depositions in high elevations (Fig.

464     9b): dust particles reaching the high mountains are small in size and difficult to deposit through gravitational

465     effects. Wet deposition is a more efficient way of depositing small particles as they collect dust in raindrops.

466     In contrast, the dry depositions play predominant roles (more than 80% in frequency) in all the other types

467     (Fig. 10a). Figure 10b further shows the contribution of wet deposition increases with deposition intensity.

468     The averaged contribution of wet depositions in magnitude increases from 19% in all events to 29% in the

469     top 10 percentile, 36% in the top 5 percentile, and 56% in the top 1 percentile largest events, supporting

470     our conclusion that wet deposition is a more efficient way of dust deposition.
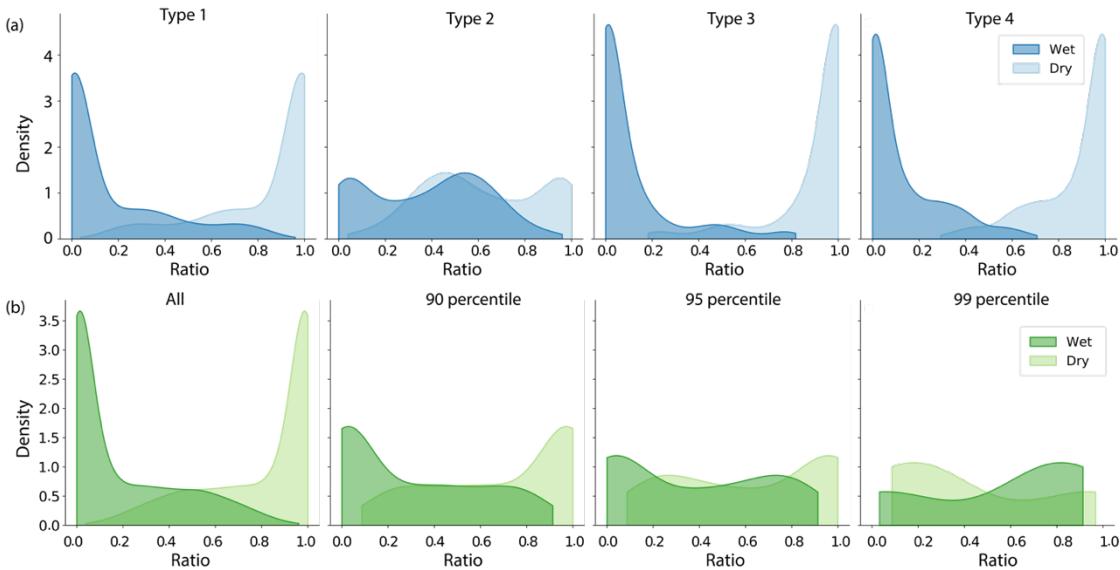
471
472   **Figure 10** (a) Distribution of contribution of wet and dry depositions to total deposition in each type in
473   WRF-Chem. (b) Distribution of contribution of wet and dry depositions to total deposition for all
474   depositions, depositions over 90th, 95th, and 99th percentile.
475

476 **3.4 Features of the dust transport in MERRA-2**

477     We repeated the SOM analyses using 2019 MERRA-2 data to examine the WRF-Chem model

478 performance and interannual variability. We conducted additional SOM analyses using 200111-2021

479 climatology MERRA-2 data to investigate the interannual variability of the transport patterns. The low-

480 level and mid-level dust transport features identified in MERRA-2 (Figs. 11-12) are similar to their

481 corresponding types in WRF-Chem (Fig. 3), with types 1, 2, 3, and 4 representing MSR, SBJ-related, NPH-

482 related and CPZ transport, respectively (Fig. 11). Additionally, north-south transport occurs in the middle

483 layer in type 3 and west-east transport in type 4, despite the slight difference in the peak region (Fig. 12).
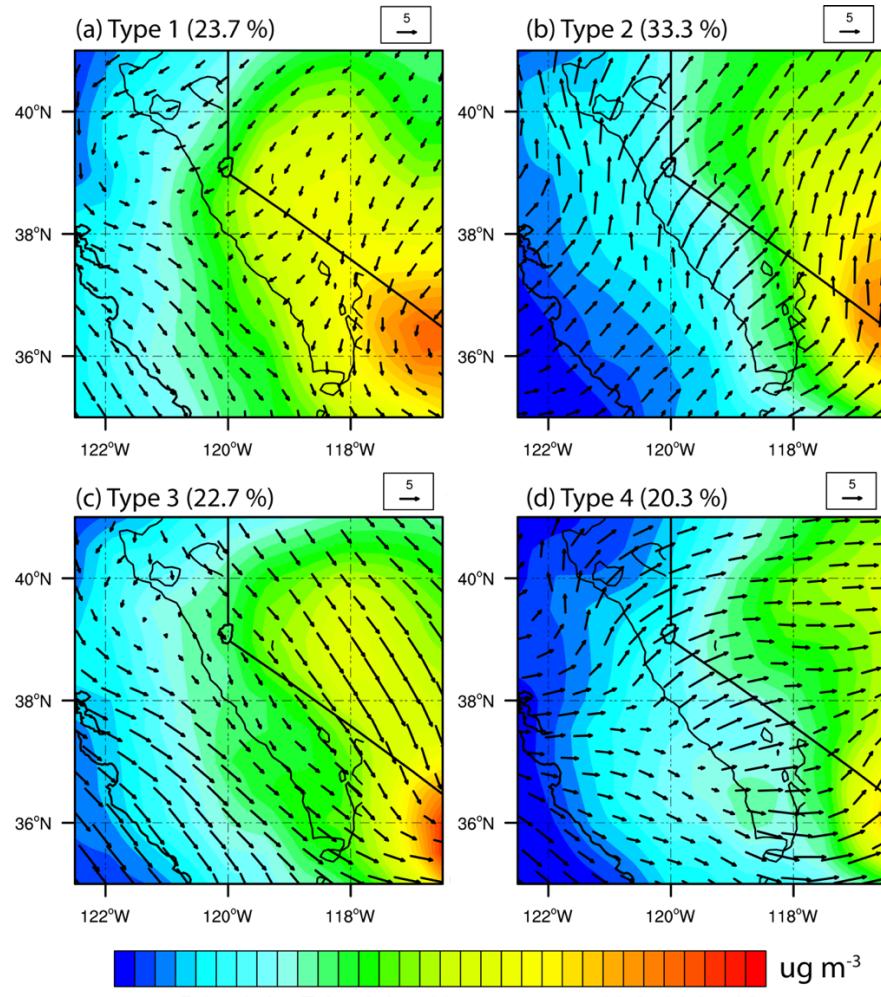
484
485 **Figure 11** Low-level dust concentration (ug m⁻³) and wind vectors (m s⁻¹) in each of the four SOM types
486 from MERRA-2 for the year 2019. The numbers on the top of subplots denote the frequency of each type.
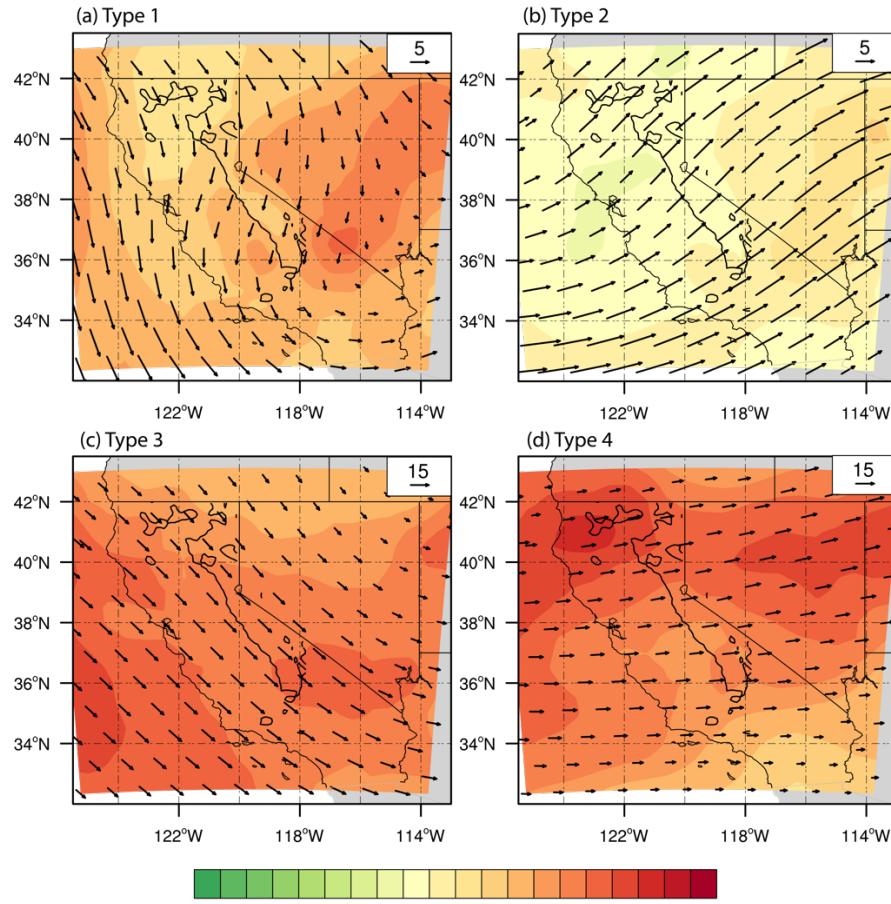
**Figure 12** Mid-level (200-700 hPa average) dust concentration (ug m⁻³) and dust transport fluxes (ug m⁻² s⁻¹) in each of the four SOM types from MERRA-2 for the year 2019

The relative contribution of each transport type in MERRA-2 (SBJ-related > MSR > CPZ > NPH-related) is generally consistent with the results in WRF-Chem (MSR > SBJ-related > CPZ > NPH-related), except that the MSR transport occurs less frequently in MERRA-2. The difference is largely caused by the spatial resolution of the two datasets. With a resolution of 0.5°×0.625°, MERRA-2 has smooth topography information and cannot resolve the high peaks of the Sierra Nevada which produce the MSR winds and transport. Consequently, MSR transport contributes to a smaller fraction in the MERRA-2. The coarser resolution MERRA-2 also produces a more homogeneous dust concentration at low levels than 2-km WRF-Chem.

Similar dust concentrations and transport patterns are found in the 21̶1̶-year SOM analysis (Fig. 13), indicating that the four patterns identified in 2019 are representative of the climatological conditions.

501 In climatology, the SBJ is weaker and air inflows hit the California coast at a further north latitude (about

502 40 °N; Fig. 13b), which is reasonable as 2019 is an El Niño year with stronger AR reaching California

503 further south than usual.

504 The changes in the transport patterns reflect the interannual variations of large-scale forcings and

505 regional weather conditions, which is investigated using the frequency of each type in a year during 2001-

506 2021 (Fig. S4). Types 1 and 4 have a negative correlation coefficient (R=-0.75) in their frequency,

507 indicating the competing impact between remote transport and local emissions on dust concentrations over

508 the Sierra Nevada. Especially, type 4 tends to occur more frequently during La Niña years while less

509 frequently during El Niño years. An opposite conclusion can be drawn for type 1.

510 We further examine the dust transport pattern and the frequency of the four SOM types during three

511 La Niña (2008, 2011, and 2021) and three El Niño (2015, 2016, and 2019) years. We find that the La Niña

512 years have larger dust concentrations than El Niño years in both lower levels and middle levels (Figs. S5-

513 S8), due to suppressed precipitations and drier soil in the southwestern U.S. Meanwhile, the frequencies of

514 types 3 and 4 are higher in El Niño years, reflecting the increased contribution of cross-Pacific transport to

515 dust loading over California. The increase of remote transport weakens the relative importance of local

516 emissions, decreasing the frequency of type 1.
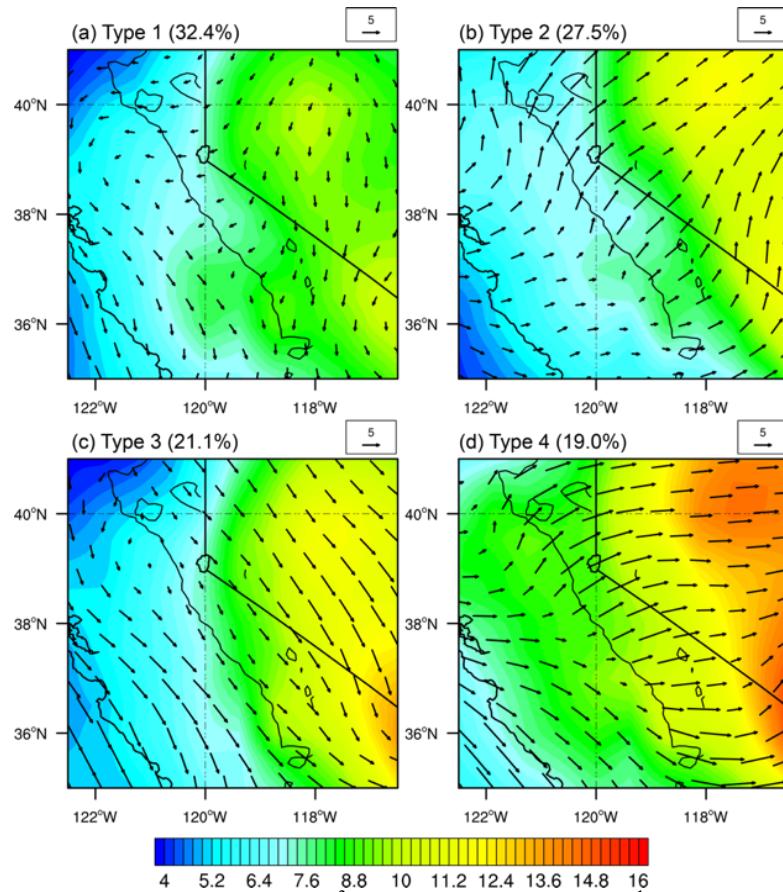
**Figure 13** Low level dust concentration (ug m$^{-3}$) and wind vectors (m s$^{-1}$) in each of the four SOM types from MERRA-2 averaged over 2001-2021. The numbers on the top right of subplots denote the frequency of each type.

## 4. Conclusions and discussion

523
524  **Figure 14** Schematic diagram of typical dust transport patterns across the Sierra Nevada. The "MSR"
525  demotes mesoscale regional transport. The "SBJ" and "NPH" denotes dust transport dominated by Sierra-
526  Barrier Jets (SBJ) and North Pacific High (NPH), respectively, while the "CPZ" denotes Cross-Pacific
527  Zonal transport.
528

529        With a focus on the dust that influences the mountain snow, we investigated the dust sources

530  surrounding the Sierra Nevada and their typical transport patterns during the spring and early summer.

531  Despite the strongest emissions from the Mojave Desert, dust is only transported northward to the mountain

532  when the mesoscale weather pattern dominates the southwest U.S. (Fig. 14). During 64.25% of our study

533  period, dust from the Mojave Desert is transported away from the mountains. Dust emitted from the Great

534  Basin is transported to the central Sierra Nevada during MSR transport and to the eastern part when the

535  NPH builds in the eastern Pacific. It is blown eastward by air inflows from the ocean during SBJ or cross-

536  Pacific transport. In contrast, dust produced by the Central Valley is persistently transported to the west

537    mountain slope, playing an essential role in snow impurities there. Carried by intense air inflows, it can be

538    transported to the lee-side of the Sierra Nevada .

539    During April, Asia dust is transported zonally over the North Pacific through the straight zonal

540    isobars at the middle level. The dust layer descends to 800 hPa when it reaches the California coast. In the

541    presence of the NPH, dust emitted from Asia excurses north into Alaska/Canada and travels south along

542    the U.S. west coast. The dust travels at a higher altitude, and the concentrations are weaker than the zonal

543    transport.

544    Large amounts of depositions are found on the west slope, which generally decrease with elevations.

545    Dust particles transported to the higher altitude are small in size and difficult to deposit through gravitational

546    effects. The SBJ-produced AR collects dust in the rain and snow and deposits it on the high mountain.

547    Besides, considerable depositions occur when the elevated dust layer from the Pacific collides with the

548    mountain.We acknowledge that our characterization of dominant transport patterns might be limited by

549    model uncertainties. Besides, the coarse-resolution reanalyses data, MERRA-2, cannot accurately resolve

550    the topography effects and tends to underestimate mesoscale regional transport. Furthermore, both WRF-

551    Chem and MERRA-2 describe dust emissions from dryland by relating them to high wind speed, soil

552    moisture, and soil type (Ginoux et al., 2001), while dust emission from agricultural lands is not specifically

553    implemented. However, a comprehensive evaluation of airborne dust and PM2.5 concentration between

554    model simulation and site observations in our previous study shows a good agreement between both (Huang

555    et al., 2022a). In addition, the dust transport pathways have well-defined patterns associated with the

556    mesoscale and large-scale weather systems. The general consistency across different models (WRF-Chem

557    and MERRA-2) and observations (satellite analysis) and across different years also give us confidence that

558    the results are valid despite model uncertainties.

559    The analyses of dust emission and transport can be used to understand dust transport in a changing

560    climate. Studies have shown that global warming continues to dry the soil, producing more dust emissions

561    over the western U.S. Nevertheless, the change in transport and deposition patterns has not been well

562    recognized. Our study highlighted the connection between dust transport and dominant weather patterns

563 across the Sierra Nevada; the latter might respond in a more predictable way to climate change. Future

564 projections show that global warming may increase the frequency of landfalling AR by 20-35% by the end

565 of the 21$^{st}$ century (Hagos et al., 2016; Rhoades et al., 2021). Besides, the widening of the Hadley Cell in

566 response to global warming might enhance the NPH and shift it poleward (Song et al., 2018; Choi et al.,

567 2016). Thus said, the SBJ- and NPH-related dust transport may occur more frequently while the MSR

568 transport may become less common. In this regard, changes in dust emissions from the Central Valley might

569 play a more critical role in mountain snow impurities than those from the Mojave Desert and the Great

570 Basin, producing more depositions on the west slope of the Sierra Nevada.

571

572 **Data availability:**

573 The IASI DOD data is acquired from https://iasi.aeris-data.fr/dust-aod/. The MIDAS DOD is acquired from

574 https://zenodo.org/record/4244106#.YsJqe-zMIws. MERRA-2 aerosol reanalyses are available from

575 https://disc.gsfc.nasa.gov/datasets?keywords=MERRA2&page=1 and ERA5 wind reanalyses are available

576 from https://rda.ucar.edu/datasets/ds633.0/. The WRF-Chem and MERRA-2 SOM clustering results have

577 been uploaded to https://doi.org/10.5281/zenodo.6795994.

578

579 **Author contributions:**

580 HH performed the analysis and drafted the manuscript. The methodology was developed by HH and YL.

581 JZ and AG provided the observational data used for model validation. YQ, CH, and ZZ helped with the

582 analysis and offered valuable comments. All authors contributed to writing and editing the manuscript.

583

584 **Competing interests:**

585 The authors declare that they have no conflict of interest.

586

587 **Acknowledgement:**

588    This research was supported by NASA awards: 80NSSC21K0997, 80NSSC20K1722, 80NSSC20K1349,

589    and 80NSSC18K1489. Antonis Gkikas was supported by the Hellenic Foundation for Research and

590    Innovation (H.F.R.I.) under the "2nd Call for H.F.R.I. Research Projects to support Post-Doctoral

591    Researchers" (project acronym: ATLANTAS, project number: 544). The Pacific Northwest National

592    Laboratory (PNNL) is operated for DOE by the Battelle Memorial Institute under contract DE-AC05-

593    76RLO1830.

594  Reference:

595  Aarons, S. M., Arvin, L. J., Aciego, S. M., Riebe, C. S., Johnson, K. R., Blakowski, M. A., Koornneef,
596  J. M., Hart, S. C., Barnes, M. E., Dove, N., Botthoff, J. K., Maltz, M., and Aronson, E. L.: Competing
597  droughts affect dust delivery to Sierra Nevada, Aeolian Research, 41, 100545,
598  https://doi.org/10.1016/j.aeolia.2019.100545, 2019.
599  Achakulwisut, P., Shen, L., and Mickley, L. J.: What Controls Springtime Fine Dust Variability in the
600  Western United States? Investigating the 2002–2015 Increase in Fine Dust in the U.S. Southwest,
601  Journal of Geophysical Research: Atmospheres, 122, 12,449-412,467,
602  https://doi.org/10.1002/2017JD027208, 2017.
603  Aciego, S. M., Riebe, C. S., Hart, S. C., Blakowski, M. A., Carey, C. J., Aarons, S. M., Dove, N. C.,
604  Botthoff, J. K., Sims, K. W. W., and Aronson, E. L.: Dust outpaces bedrock in nutrient supply to
605  montane forest ecosystems, Nat Commun, 8, 14800, 10.1038/ncomms14800, 2017.
606  Ault, A. P., Williams, C. R., White, A. B., Neiman, P. J., Creamean, J. M., Gaston, C. J., Ralph, F. M.,
607  and Prather, K. A.: Detection of Asian dust in California orographic precipitation, Journal of
608  Geophysical Research: Atmospheres, 116, https://doi.org/10.1029/2010JD015351, 2011.
609  Bao, J.-W., Michelson, S. A., Persson, P. O. G., Djalalova, I. V., and Wilczak, J. M.: Observed and
610  WRF-Simulated Low-Level Winds in a High-Ozone Episode during the Central California Ozone
611  Study, Journal of Applied Meteorology and Climatology, 47, 2372-2394,
612  10.1175/2008jamc1822.1, 2008.
613  Bao, M. and Wallace, J. M.: Cluster Analysis of Northern Hemisphere Wintertime 500-hPa Flow
614  Regimes during 1920–2014, J Atmos Sci, 72, 3597-3608, 10.1175/JAS-D-15-0001.1, 2015.
615  Brahney, J., Ballantyne, A. P., Sievers, C., and Neff, J. C.: Increasing Ca2+ deposition in the western
616  US: The role of mineral aerosols, Aeolian Research, 10, 77-87,
617  https://doi.org/10.1016/j.aeolia.2013.04.003, 2013.
618  Buchard, V., da Silva, A. M., Randles, C. A., Colarco, P., Ferrare, R., Hair, J., Hostetler, C., Tackett,
619  J., and Winker, D.: Evaluation of the surface PM2.5 in Version 1 of the NASA MERRA Aerosol
620  Reanalysis over the United States, Atmos Environ, 125, 100-111,
621  https://doi.org/10.1016/j.atmosenv.2015.11.004, 2016.
622  Buchard, V., Randles, C. A., da Silva, A. M., Darmenov, A., Colarco, P. R., Govindaraju, R., Ferrare,
623  R., Hair, J., Beyersdorf, A. J., Ziemba, L. D., and Yu, H.: The MERRA-2 Aerosol Reanalysis, 1980
624  Onward. Part II: Evaluation and Case Studies, J Climate, 30, 6851-6872, 10.1175/JCLI-D-16-0613.1,
625  2017.
626  Buchholz, R., Emmons, L., and Tilmes, S.: CESM2. 1/CAM-chem instantaneous output for
627  boundary conditions, in: UCAR/NCAR-Atmospheric Chemistry Observations and Modeling
628  Laboratory, 2019.
629  Capelle, V., Chédin, A., Pondrom, M., Crevoisier, C., Armante, R., Crepeau, L., and Scott, N. A.:
630  Infrared dust aerosol optical depth retrieved daily from IASI and comparison with AERONET over
631  the period 2007–2016, Remote Sens Environ, 206, 15-32,
632  https://doi.org/10.1016/j.rse.2017.12.008, 2018.
633  Capelle, V., Chédin, A., Siméon, M., Tsamalis, C., Pierangelo, C., Pondrom, M., Crevoisier, C.,
634  Crepeau, L., and Scott, N. A.: Evaluation of IASI-derived dust aerosol characteristics over the
635  tropical belt, Atmos. Chem. Phys., 14, 9343-9362, 10.5194/acp-14-9343-2014, 2014.

Chapman, E. G., Gustafson, W. I., Easter, R. C., Barnard, J. C., Ghan, S. J., Pekour, M. S., and Fast, J. D.: Coupling aerosol-cloud-radiative processes in the WRF-Chem model: Investigating the radiative impact of elevated point sources, Atmos Chem Phys, 9, 945-964, 10.5194/acp-9-945-2009, 2009.

Chin, M., Diehl, T., Ginoux, P., and Malm, W.: Intercontinental transport of pollution and dust aerosols: implications for regional air quality, Atmos. Chem. Phys., 7, 5501-5517, 10.5194/acp-7-5501-2007, 2007.

Chin, M., Ginoux, P., Kinne, S., Torres, O., Holben, B. N., Duncan, B. N., Martin, R. V., Logan, J. A., Higurashi, A., and Nakajima, T.: Tropospheric Aerosol Optical Thickness from the GOCART Model and Comparisons with Satellite and Sun Photometer Measurements, J Atmos Sci, 59, 461-483, 10.1175/1520-0469(2002)059<0461:Taotft>2.0.Co;2, 2002.

Choi, J., Lu, J., Son, S. W., Frierson, D. M., and Yoon, J. H.: Uncertainty in future projections of the North Pacific subtropical high and its implication for California winter precipitation change, Journal of Geophysical Research: Atmospheres, 121, 795-806, 2016.

Clausnitzer, H. and Singer, M. J.: Environmental influences on respirable dust production from agricultural operations in California, Atmos Environ, 34, 1739-1745, https://doi.org/10.1016/S1352-2310(99)00385-4, 2000.

Creamean, J. M., Spackman, J. R., Davis, S. M., and White, A. B.: Climatology of long-range transported Asian dust along the West Coast of the United States, Journal of Geophysical Research: Atmospheres, 119, 12,171-112,185, https://doi.org/10.1002/2014JD021694, 2014.

Creamean, J. M., Suski, K. J., Rosenfeld, D., Cazorla, A., DeMott, P. J., Sullivan, R. C., White, A. B., Ralph, F. M., Minnis, P., and Comstock, J. M.: Dust and biological aerosols from the Sahara and Asia influence precipitation in the western US, Science, 339, 1572-1578, 2013.

Crooks, J. L., Cascio, W. E., Percy, M. S., Reyes, J., Neas, L. M., and Hilborn, E. D.: The Association between Dust Storms and Daily Non-Accidental Mortality in the United States, 1993–2005, Environ Health Persp, 124, 1735-1743, doi:10.1289/EHP216, 2016.

Duniway, M. C., Pfennigwerth, A. A., Fick, S. E., Nauman, T. W., Belnap, J., and Barger, N. N.: Wind erosion and dust from US drylands: a review of causes, consequences, and solutions in a changing world, Ecosphere, 10, e02650, https://doi.org/10.1002/ecs2.2650, 2019.

Easter, R. C., Ghan, S. J., Zhang, Y., Saylor, R. D., Chapman, E. G., Laulainen, N. S., Abdul-Razzak, H., Leung, L. R., Bian, X. D., and Zaveri, R. A.: MIRAGE: Model description and evaluation of aerosols and trace gases, J Geophys Res-Atmos, 109, Artn D20210
10.1029/2004jd004571, 2004.

Emmons, L. K., Schwantes, R. H., Orlando, J. J., Tyndall, G., Kinnison, D., Lamarque, J. F., Marsh, D., Mills, M. J., Tilmes, S., Bardeen, C., Buchholz, R. R., Conley, A., Gettelman, A., Garcia, R., Simpson, I., Blake, D. R., Meinardi, S., and Petron, G.: The Chemistry Mechanism in the Community Earth System Model Version 2 (CESM2), J Adv Model Earth Sy, 12, e2019MS001882, ARTN e2019MS001882
10.1029/2019MS001882, 2020.

Forster, P., Ramaswamy, V., Artaxo, P., Berntsen, T., Betts, R., Fahey, D. W., Haywood, J., Lean, J., Lowe, D. C., and Myhre, G.: Changes in atmospheric constituents and in radiative forcing. Chapter 2, in: Climate change 2007. The physical science basis, 2007.

Gelaro, R., McCarty, W., Suarez, M. J., Todling, R., Molod, A., Takacs, L., Randles, C., Darmenov, A., Bosilovich, M. G., Reichle, R., Wargan, K., Coy, L., Cullather, R., Draper, C., Akella, S., Buchard,

V., Conaty, A., da Silva, A., Gu, W., Kim, G. K., Koster, R., Lucchesi, R., Merkova, D., Nielsen, J. E., Partyka, G., Pawson, S., Putman, W., Rienecker, M., Schubert, S. D., Sienkiewicz, M., and Zhao, B.: The Modern-Era Retrospective Analysis for Research and Applications, Version 2 (MERRA-2), J Clim, Volume 30, 5419-5454, 10.1175/JCLI-D-16-0758.1, 2017.

Giannadaki, D., Pozzer, A., and Lelieveld, J.: Modeled global effects of airborne desert dust on air quality and premature mortality, Atmos Chem Phys, 14, 957-968, 2014.

Ginoux, P., Prospero, J. M., Gill, T. E., Hsu, N. C., and Zhao, M.: Global-scale attribution of anthropogenic and natural dust sources and their emission rates based on MODIS Deep Blue aerosol products, Reviews of Geophysics, 50, https://doi.org/10.1029/2012RG000388, 2012.

Ginoux, P., Chin, M., Tegen, I., Prospero, J. M., Holben, B., Dubovik, O., and Lin, S. J.: Sources and distributions of dust aerosols simulated with the GOCART model, J Geophys Res-Atmos, 106, 20255-20273, Doi 10.1029/2000jd000053, 2001.

Gkikas, A., Proestakis, E., Amiridis, V., Kazadzis, S., Di Tomaso, E., Marinou, E., Hatzianastassiou, N., Kok, J. F., and García-Pando, C. P.: Quantification of the dust optical depth across spatiotemporal scales with the MIDAS global dataset (2003–2017), Atmos. Chem. Phys., 22, 3553-3578, 10.5194/acp-22-3553-2022, 2022.

Gkikas, A., Proestakis, E., Amiridis, V., Kazadzis, S., Di Tomaso, E., Tsekeri, A., Marinou, E., Hatzianastassiou, N., and Pérez García-Pando, C.: ModIs Dust AeroSol (MIDAS): a global fine-resolution dust optical depth data set, Atmos. Meas. Tech., 14, 309-334, 10.5194/amt-14-309-2021, 2021.

Goldstein, H. L., Breit, G. N., and Reynolds, R. L.: Controls on the chemical composition of saline surface crusts and emitted dust from a wet playa in the Mojave Desert (USA), J Arid Environ, 140, 50-66, https://doi.org/10.1016/j.jaridenv.2017.01.010, 2017.

Hagos, S. M., Leung, L. R., Yoon, J.-H., Lu, J., and Gao, Y.: A projection of changes in landfalling atmospheric river frequency and extreme precipitation over western North America from the Large Ensemble CESM simulations, Geophys Res Lett, 43, 1357-1363, https://doi.org/10.1002/2015GL067392, 2016.

Hand, J. L., Gill, T. E., and Schichtel, B. A.: Spatial and seasonal variability in fine mineral dust and coarse aerosol mass at remote sites across the United States, Journal of Geophysical Research: Atmospheres, 122, 3080-3097, https://doi.org/10.1002/2016JD026290, 2017.

Hand, J. L., White, W. H., Gebhart, K. A., Hyslop, N. P., Gill, T. E., and Schichtel, B. A.: Earlier onset of the spring fine dust season in the southwestern United States, Geophys Res Lett, 43, 4001-4009, https://doi.org/10.1002/2016GL068519, 2016.

Hannachi, A.: On the origin of planetary-scale extratropical winter circulation regimes, J Atmos Sci, 67, 1382-1401, 2010.

Haywood, J. M., Allan, R. P., Culverwell, I., Slingo, T., Milton, S., Edwards, J., and Clerbaux, N.: Can desert dust explain the outgoing longwave radiation anomaly over the Sahara during July 2003?, Journal of Geophysical Research: Atmospheres, 110, https://doi.org/10.1029/2004JD005232, 2005.

Hersbach, H., Bell, B., Berrisford, P., Hirahara, S., Horanyi, A., Munoz-Sabater, J., Nicolas, J., Peubey, C., Radu, R., Schepers, D., Simmons, A., Soci, C., Abdalla, S., Abellan, X., Balsamo, G., Bechtold, P., Biavati, G., Bidlot, J., Bonavita, M., De Chiara, G., Dahlgren, P., Dee, D., Diamantakis, M., Dragani, R., Flemming, J., Forbes, R., Fuentes, M., Geer, A., Haimberger, L., Healy, S., Hogan, R. J., Holm, E., Janiskova, M., Keeley, S., Laloyaux, P., Lopez, P., Lupu, C., Radnoti, G., de Rosnay,

724 P., Rozum, I., Vamborg, F., Villaume, S., and Thepaut, J. N.: The ERA5 global reanalysis, Q J Roy
725 Meteor Soc, 146, 1999-2049, 10.1002/qj.3803, 2020.

726 Hilton, F., Armante, R., August, T., Barnet, C., Bouchard, A., Camy-Peyret, C., Capelle, V., Clarisse,
727 L., Clerbaux, C., Coheur, P. F., Collard, A., Crevoisier, C., Dufour, G., Edwards, D., Faijan, F., Fourrie,
728 N., Gambacorta, A., Goldberg, M., Guidard, V., Hurtmans, D., Illingworth, S., Jacquinet-Husson,
729 N., Kerzenmacher, T., Klaes, D., Lavanant, L., Masiello, G., Matricardi, M., McNally, A., Newman,
730 S., Pavelin, E., Payan, S., Pequignot, E., Peyridieu, S., Phulpin, T., Remedios, J., Schlussel, P., Serio,
731 C., Strow, L., Stubenrauch, C., Taylor, J., Tobin, D., Wolf, W., and Zhou, D.: HYPERSPECTRAL EARTH
732 OBSERVATION FROM IASI Five Years of Accomplishments, B Am Meteorol Soc, 93, 347-370,
733 10.1175/Bams-D-11-00027.1, 2012.

734 Huang, H., Gu, Y., Xue, Y., Jiang, J., and Zhao, B.: Assessing aerosol indirect effect on clouds and
735 regional climate of East/South Asia and West Africa using NCEP GFS, Clim Dyn, 52, 5759-5774,
736 10.1007/s00382-018-4476-9, 2019.

737 Huang, H., Qian, Y., He, C., Bair, E. H., and Rittger, K.: Snow Albedo Feedbacks Enhance Snow
738 Impurity-Induced Radiative Forcing in the Sierra Nevada, Geophys Res Lett, 49, e2022GL098102,
739 https://doi.org/10.1029/2022GL098102, 2022a.

740 Huang, H., Fischella, M. R., Liu, Y., Ban, Z., Fayne, J. V., Li, D., Cavanaugh, K. C., and Lettenmaier,
741 D. P.: Changes in Mechanisms and Characteristics of Western U.S. Floods Over the Last Sixty Years,
742 Geophys Res Lett, 49, e2021GL097022, 10.1029/2021gl097022, 2022b.

743 Hunt, W. H., Winker, D. M., Vaughan, M. A., Powell, K. A., Lucker, P. L., and Weimer, C.: CALIPSO
744 Lidar Description and Performance Assessment, Journal of Atmospheric and Oceanic Technology,
745 26, 1214-1228, 10.1175/2009jtecha1223.1, 2009.

746 Jardine, G. E., Crocker, A. J., Bailey, I., Cooper, M. J., Milton, J. A., and Wilson, P. A.: The imprint
747 of windblown dust from the North American Southwest on the California Channel Islands and
748 Pacific Ocean sediments, Quaternary Science Reviews, 261, 106934,
749 https://doi.org/10.1016/j.quascirev.2021.106934, 2021.

750 Kim, D., Chin, M., Cruz, C. A., Tong, D., and Yu, H.: Spring Dust in Western North America and Its
751 Interannual Variability—Understanding the Role of Local and Transported Dust, Journal of
752 Geophysical Research: Atmospheres, 126, e2021JD035383,
753 https://doi.org/10.1029/2021JD035383, 2021.

754 Kim, M. H., Omar, A. H., Tackett, J. L., Vaughan, M. A., Winker, D. M., Trepte, C. R., Hu, Y., Liu, Z.,
755 Poole, L. R., Pitts, M. C., Kar, J., and Magill, B. E.: The CALIPSO version 4 automated aerosol
756 classification and lidar ratio selection algorithm, Atmos. Meas. Tech., 11, 6107-6135,
757 10.5194/amt-11-6107-2018, 2018.

758 Laden, F., Schwartz, J., Speizer, F. E., and Dockery, D. W.: Reduction in fine particulate air pollution
759 and mortality: Extended follow-up of the Harvard Six Cities study, Am J Respir Crit Care Med, 173,
760 667-672, 10.1164/rccm.200503-443OC, 2006.

761 Lei, H. and Wang, J. X. L.: Observed characteristics of dust storm events over the western United
762 States using meteorological, satellite, and air quality measurements, Atmos. Chem. Phys., 14,
763 7847-7857, 10.5194/acp-14-7847-2014, 2014.

764 Lim, S. S., Vos, T., Flaxman, A. D., Danaei, G., Shibuya, K., Adair-Rohani, H., AlMazroa, M. A.,
765 Amann, M., Anderson, H. R., Andrews, K. G., Aryee, M., Atkinson, C., Bacchus, L. J., Bahalim, A.
766 N., Balakrishnan, K., Balmes, J., Barker-Collo, S., Baxter, A., Bell, M. L., Blore, J. D., Blyth, F., Bonner,
767 C., Borges, G., Bourne, R., Boussinesq, M., Brauer, M., Brooks, P., Bruce, N. G., Brunekreef, B.,

Bryan-Hancock, C., Bucello, C., Buchbinder, R., Bull, F., Burnett, R. T., Byers, T. E., Calabria, B., Carapetis, J., Carnahan, E., Chafe, Z., Charlson, F., Chen, H., Chen, J. S., Cheng, A. T.-A., Child, J. C., Cohen, A., Colson, K. E., Cowie, B. C., Darby, S., Darling, S., Davis, A., Degenhardt, L., Dentener, F., Des Jarlais, D. C., Devries, K., Dherani, M., Ding, E. L., Dorsey, E. R., Driscoll, T., Edmond, K., Ali, S. E., Engell, R. E., Erwin, P. J., Fahimi, S., Falder, G., Farzadfar, F., Ferrari, A., Finucane, M. M., Flaxman, S., Fowkes, F. G. R., Freedman, G., Freeman, M. K., Gakidou, E., Ghosh, S., Giovannucci, E., Gmel, G., Graham, K., Grainger, R., Grant, B., Gunnell, D., Gutierrez, H. R., Hall, W., Hoek, H. W., Hogan, A., Hosgood, H. D., Hoy, D., Hu, H., Hubbell, B. J., Hutchings, S. J., Ibeanusi, S. E., Jacklyn, G. L., Jasrasaria, R., Jonas, J. B., Kan, H., Kanis, J. A., Kassebaum, N., Kawakami, N., Khang, Y.-H., Khatibzadeh, S., Khoo, J.-P., Kok, C., Laden, F., Lalloo, R., Lan, Q., Lathlean, T., Leasher, J. L., Leigh, J., Li, Y., Lin, J. K., Lipshultz, S. E., London, S., Lozano, R., Lu, Y., Mak, J., Malekzadeh, R., Mallinger, L., Marcenes, W., March, L., Marks, R., Martin, R., McGale, P., McGrath, J., Mehta, S., Memish, Z. A., Mensah, G. A., Merriman, T. R., Micha, R., Michaud, C., Mishra, V., Hanafiah, K. M., Mokdad, A. A., Morawska, L., Mozaffarian, D., Murphy, T., Naghavi, M., Neal, B., Nelson, P. K., Nolla, J. M., Norman, R., Olives, C., Omer, S. B., Orchard, J., Osborne, R., Ostro, B., Page, A., Pandey, K. D., Parry, C. D. H., Passmore, E., Patra, J., Pearce, N., Pelizzari, P. M., Petzold, M., Phillips, M. R., Pope, D., Pope, C. A., Powles, J., Rao, M., Razavi, H., Rehfuess, E. A., Rehm, J. T., Ritz, B., Rivara, F. P., Roberts, T., Robinson, C., Rodriguez-Portales, J. A., Romieu, I., Room, R., Rosenfeld, L. C., Roy, A., Rushton, L., Salomon, J. A., Sampson, U., Sanchez-Riera, L., Sanman, E., Sapkota, A., Seedat, S., Shi, P., Shield, K., Shivakoti, R., Singh, G. M., Sleet, D. A., Smith, E., Smith, K. R., Stapelberg, N. J. C., Steenland, K., Stöckl, H., Stovner, L. J., Straif, K., Straney, L., Thurston, G. D., Tran, J. H., Van Dingenen, R., van Donkelaar, A., Veerman, J. L., Vijayakumar, L., Weintraub, R., Weissman, M. M., White, R. A., Whiteford, H., Wiersma, S. T., Wilkinson, J. D., Williams, H. C., Williams, W., Wilson, N., Woolf, A. D., Yip, P., Zielinski, J. M., Lopez, A. D., Murray, C. J. L., and Ezzati, M.: A comparative risk assessment of burden of disease and injury attributable to 67 risk factors and risk factor clusters in 21 regions, 1990–2010: a systematic analysis for the Global Burden of Disease Study 2010, The Lancet, 380, 2224-2260, https://doi.org/10.1016/S0140-6736(12)61766-8, 2012.

Liu, Y., Qian, Y., and Berg, L. K.: Local-thermal-gradient and large-scale-circulation impacts on turbine-height wind speed forecasting over the Columbia River Basin, Wind Energ. Sci., 7, 37-51, 10.5194/wes-7-37-2022, 2022.

Muhs, D. R., Budahn, J., Reheis, M., Beann, J., Skipp, G., and Fisher, E.: Airborne dust transport to the eastern Pacific Ocean off southern California: Evidence from San Clemente Island, Journal of Geophysical Research: Atmospheres, 112, https://doi.org/10.1029/2006JD007577, 2007.

Neff, J. C., Ballantyne, A. P., Farmer, G. L., Mahowald, N. M., Conroy, J. L., Landry, C. C., Overpeck, J. T., Painter, T. H., Lawrence, C. R., and Reynolds, R. L.: Increasing eolian dust deposition in the western United States linked to human activity, Nat Geosci, 1, 189-195, 10.1038/ngeo133, 2008.

Neiman, P. J., Hughes, M., Moore, B. J., Ralph, F. M., and Sukovich, E. M.: Sierra Barrier Jets, Atmospheric Rivers, and Precipitation Characteristics in Northern California: A Composite Perspective Based on a Network of Wind Profilers, Mon Weather Rev, 141, 4211-4233, 10.1175/mwr-d-13-00112.1, 2013.

Okin, G., Gillette, D., and Herrick, J.: Multi-scale controls on and consequences of aeolian processes in landscape change in arid and semi-arid environments, J Arid Environ, 65, 253-275, 2006.

Pappagianis, D. and Einstein, H.: Tempest from Tehachapi takes toll or Coccidioides conveyed aloft and afar, Western Journal of Medicine, 129, 527, 1978.

Pu, B. and Ginoux, P.: How reliable are CMIP5 models in simulating dust optical depth?, Atmos. Chem. Phys., 18, 12491-12510, 10.5194/acp-18-12491-2018, 2018.

Qian, Y., Gustafson, W. I., Leung, L. R., and Ghan, S. J.: Effects of soot-induced snow albedo change on snowpack and hydrological cycle in western United States based on Weather Research and Forecasting chemistry and regional climate simulations, J Geophys Res-Atmos, 114, Artn D03108 10.1029/2008jd011039, 2009.

Qian, Y., Yasunari, T. J., Doherty, S. J., Flanner, M. G., Lau, W. K. M., Ming, J., Wang, H., Wang, M., Warren, S. G., and Zhang, R.: Light-absorbing particles in snow and ice: Measurement and modeling of climatic and hydrological impact, Adv Atmos Sci, 32, 64-91, 10.1007/s00376-014-0010-0, 2014.

Randles, C. A., Da Silva, A. M., Buchard, V., Colarco, P. R., Darmenov, A., Govindaraju, R., Smirnov, A., Holben, B., Ferrare, R., Hair, J., Shinozuka, Y., and Flynn, C. J.: The MERRA-2 Aerosol Reanalysis, 1980 - onward, Part I: System Description and Data Assimilation Evaluation, J Clim, 30, 6823-6850, 10.1175/JCLI-D-16-0609.1, 2017.

Reheis, M. C. and Kihl, R.: Dust Deposition in Southern Nevada and California, 1984-1989 - Relations to Climate, Source Area, and Source Lithology, J Geophys Res-Atmos, 100, 8893-8918, Doi 10.1029/94jd03245, 1995.

Reusch, D. B., Alley, R. B., and Hewitson, B. C.: North Atlantic climate variability from a self-organizing map perspective, Journal of Geophysical Research: Atmospheres, 112, https://doi.org/10.1029/2006JD007460, 2007.

Rhoades, A. M., Risser, M. D., Stone, D. A., Wehner, M. F., and Jones, A. D.: Implications of warming on western United States landfalling atmospheric rivers and their flood damages, Weather Clim Extreme, 32, 100326, https://doi.org/10.1016/j.wace.2021.100326, 2021.

Rodionov, S. N., Bond, N. A., and Overland, J. E.: The Aleutian Low, storm tracks, and winter climate variability in the Bering Sea, Deep Sea Research Part II: Topical Studies in Oceanography, 54, 2560-2577, https://doi.org/10.1016/j.dsr2.2007.08.002, 2007.

Sarangi, C., Qian, Y., Rittger, K., Leung, L. R., Chand, D., Bormann, K. J., and Painter, T. H.: Dust dominates high-altitude snow darkening and melt over high-mountain Asia, Nat Clim Change, 10, 1045-+, 10.1038/s41558-020-00909-3, 2020.

Skiles, S. M., Flanner, M., Cook, J. M., Dumont, M., and Painter, T. H.: Radiative forcing by light-absorbing particles in snow, Nat Clim Change, 8, 964-971, 10.1038/s41558-018-0296-5, 2018.

Song, F., Leung, L. R., Lu, J., and Dong, L.: Future Changes in Seasonality of the North Pacific and North Atlantic Subtropical Highs, Geophys Res Lett, 45, 11,959-911,968, https://doi.org/10.1029/2018GL079940, 2018.

Song, F., Feng, Z., Leung, L. R., Houze Jr, R. A., Wang, J., Hardin, J., and Homeyer, C. R.: Contrasting Spring and Summer Large-Scale Environments Associated with Mesoscale Convective Systems over the U.S. Great Plains, J Climate, 32, 6749-6767, 10.1175/JCLI-D-18-0839.1, 2019.

Song, Q., Zhang, Z., Yu, H., Ginoux, P., and Shen, J.: Global dust optical depth climatology derived from CALIOP and MODIS aerosol retrievals on decadal timescales: regional and interannual variability, Atmos. Chem. Phys., 21, 13369-13395, 10.5194/acp-21-13369-2021, 2021.

854 Tong, D. Q., Wang, J. X. L., Gill, T. E., Lei, H., and Wang, B.: Intensified dust storm activity and
855 Valley fever infection in the southwestern United States, Geophys Res Lett, 44, 4304-4312,
856 https://doi.org/10.1002/2017GL073524, 2017.

857 Vicars, W. C. and Sickman, J. O.: Mineral dust transport to the Sierra Nevada, California: Loading
858 rates and potential source areas, J Geophys Res-Biogeo, 116, Artn G01018
859 10.1029/2010jg001394, 2011.

860 Vigaud, N. and Robertson, A. W.: Convection regimes and tropical–midlatitude interactions over
861 the Intra–American Seas from May to November, Int J Climatol, 37, 987-1000, 2017.

862 Vigaud, N., Robertson, A. W., and Tippett, M. K.: Predictability of recurrent weather regimes over
863 North America during winter from submonthly reforecasts, Mon Weather Rev, 146, 2559-2577,
864 2018.

865 Visbeck, M. H., Hurrell, J. W., Polvani, L., and Cullen, H. M.: The North Atlantic Oscillation: past,
866 present, and future, Proceedings of the National Academy of Sciences, 98, 12876-12877, 2001.

867 von Storch, H., Langenberg, H., and Feser, F.: A spectral nudging technique for dynamical
868 downscaling purposes, Mon Weather Rev, 128, 3664-3673, 2000.

869 Voss, K. K. and Evan, A. T.: A New Satellite-Based Global Climatology of Dust Aerosol Optical
870 Depth, Journal of Applied Meteorology and Climatology, 59, 83-102, 10.1175/JAMC-D-19-0194.1,
871 2020.

872 Voss, K. K., Evan, A. T., and Ralph, F. M.: Evaluating the Meteorological Conditions Associated
873 With Dusty Atmospheric Rivers, Journal of Geophysical Research: Atmospheres, 126,
874 e2021JD035403, https://doi.org/10.1029/2021JD035403, 2021.

875 Winker, D. M., Vaughan, M. A., Omar, A., Hu, Y. X., Powell, K. A., Liu, Z. Y., Hunt, W. H., and Young,
876 S. A.: Overview of the CALIPSO Mission and CALIOP Data Processing Algorithms, Journal of
877 Atmospheric and Oceanic Technology, 26, 2310-2323, 10.1175/2009jtecha1281.1, 2009.

878 Winker, D. M., Pelon, J., Coakley, J. A., Ackerman, S. A., Charlson, R. J., Colarco, P. R., Flamant, P.,
879 Fu, Q., Hoff, R. M., Kittaka, C., Kubar, T. L., Le Treut, H., McCormick, M. P., Megie, G., Poole, L.,
880 Powell, K., Trepte, C., Vaughan, M. A., and Wielicki, B. A.: THE CALIPSO MISSION A Global 3D View
881 of Aerosols and Clouds, B Am Meteorol Soc, 91, 1211-1229, 10.1175/2010bams3009.1, 2010.

882 Wu, L. T., Su, H., Kalashnikova, O. V., Jiang, J. H., Zhao, C., Garay, M. J., Campbell, J. R., and Yu, N.
883 P.: WRF-Chem simulation of aerosol seasonal variability in the San Joaquin Valley, Atmos Chem
884 Phys, 17, 7291-7309, 10.5194/acp-17-7291-2017, 2017.

885 Wu, L. T., Gu, Y., Jiang, J. H., Su, H., Yu, N. P., Zhao, C., Qian, Y., Zhao, B., Liou, K. N., and Choi, Y.
886 S.: Impacts of aerosols on seasonal precipitation and snowpack in California based on convection-
887 permitting WRF-Chem simulations, Atmos Chem Phys, 18, 5529-5547, 10.5194/acp-18-5529-
888 2018, 2018.

889 Young, S. A., Vaughan, M. A., Garnier, A., Tackett, J. L., Lambeth, J. D., and Powell, K. A.: Extinction
890 and optical depth retrievals for CALIPSO's Version 4 data release, Atmospheric Measurement
891 Techniques, 11, 5701-5727, 10.5194/amt-11-5701-2018, 2018.

892 Yu, H., Tan, Q., Chin, M., Remer, L. A., Kahn, R. A., Bian, H., Kim, D., Zhang, Z., Yuan, T., Omar, A.
893 H., Winker, D. M., Levy, R. C., Kalashnikova, O., Crepeau, L., Capelle, V., and Chédin, A.: Estimates
894 of African Dust Deposition Along the Trans-Atlantic Transit Using the Decadelong Record of
895 Aerosol Measurements from CALIOP, MODIS, MISR, and IASI, Journal of Geophysical Research:
896 Atmospheres, 124, 7975-7996, https://doi.org/10.1029/2019JD030574, 2019.

897 Zaveri, R. A. and Peters, L. K.: A new lumped structure photochemical mechanism for large-scale
898 applications, Journal of Geophysical Research: Atmospheres, 104, 30387-30415, 1999.
899 Zheng, J., Zhang, Z., Garnier, A., Yu, H., Song, Q., Wang, C., Dubuisson, P., and Di Biagio, C.: The
900 thermal infrared optical depth of mineral dust retrieved from integrated CALIOP and IIR
901 observations, Remote Sens Environ, 270, 112841, https://doi.org/10.1016/j.rse.2021.112841,
902 2022.
903